



**HAL**  
open science

**Structural impact of carbon  
nanofibers/few-layer-graphene substrate decorated with  
Ni for CO<sub>2</sub> methanation via inductive heating**

Anurag Mohanty, Cuong Duong Viet, Anne-Cécile Roger, Alexandre Adam,  
Damien Mertz, Walid Baaziz, Izabela Janowska

► **To cite this version:**

Anurag Mohanty, Cuong Duong Viet, Anne-Cécile Roger, Alexandre Adam, Damien Mertz, et al..  
Structural impact of carbon nanofibers/few-layer-graphene substrate decorated with Ni for CO<sub>2</sub>  
methanation via inductive heating. *Applied Catalysis B: Environmental*, 2021, 298, pp.120589.  
10.1016/j.apcatb.2021.120589 . hal-03427140

**HAL Id: hal-03427140**

**<https://hal.science/hal-03427140>**

Submitted on 22 Nov 2021

**HAL** is a multi-disciplinary open access archive for the deposit and dissemination of scientific research documents, whether they are published or not. The documents may come from teaching and research institutions in France or abroad, or from public or private research centers.

L'archive ouverte pluridisciplinaire **HAL**, est destinée au dépôt et à la diffusion de documents scientifiques de niveau recherche, publiés ou non, émanant des établissements d'enseignement et de recherche français ou étrangers, des laboratoires publics ou privés.

# Structural impact of Carbon Nanofibers/Few-Layer-Graphene substrate decorated with Ni for CO<sub>2</sub> methanation via Inductive Heating

Anurag Mohanty <sup>a</sup>, Cuong Duong Viet <sup>a</sup>, Anne-Cécile Roger <sup>a</sup>, Alexandre Adam <sup>b</sup>, Damien Mertz <sup>b</sup>,  
Walid Baaziz <sup>b</sup>, Izabela Janowska <sup>a \*</sup>

<sup>a</sup> *Institut de Chimie et Procédés pour l'Énergie, l'Environnement et la Santé (ICPEES), CNRS UMR 7515-University of Strasbourg, 25 Rue Becquerel, 67087, Strasbourg, France*

<sup>b</sup> *Institut de Physique et de Chimie des Matériaux de Strasbourg (IPCMS), CNRS UMR 7504-University of Strasbourg, 23 rue du Loess, BP 43, 67034, Strasbourg, France*

\* *Corresponding author; Email: janowskai@unistra.fr*

## Abstract

The structure of catalyst containing Ni nanoparticles (NPs) supported over carbon nanofibers/few layer graphene (CNFs/FLG) was tailored via modification of chemical vapor deposition parameters in view of methanation of CO<sub>2</sub> under induction heating mode (IH). High edges-to- graphitic plane ratio in the support achieved due to the specific herringbone morphology of CNFs allowed to get high CO<sub>2</sub> conversion of 85% at relatively low temperature (360°C) at very low Ni loading of only 10%. A design of catalyst included also the use of FLG known for high temperature conductivity and by occasion serving as a support to grow CNFs. The performances of certain catalysts are also tested under “standard” Joule heating in order to check the role of the magnetic and conductive carbon support. The morphology, chemical composition and SAR measurements of the catalysts and carbon supports themselves are addressed and their structure-catalytic performances are discussed.

## Keywords

CO<sub>2</sub> methanation; Few-layer-graphene; Carbon nanofiber; Inductive Heating; Ni catalysts

### 1. Introduction

Recent years have seen huge spike in the global emissions of carbon dioxide (CO<sub>2</sub>) reaching the values of 36.57 billion metric tons [1]. Rapid increase in the population has paved pathways for unprecedented demands in various sectors causing various global climatic changes. Industrialisation has aided in furthering the emission of CO<sub>2</sub> gases by forming a majority share of 30%. Mitigation of such issues is of prime importance in order to have sustainable development of the society. This

brings us to the two-faceted solution at hand to not only immediately help reduce the CO<sub>2</sub> content in the atmosphere but also to convert it into a form which can be utilised as renewable energy. Catalytic hydrogenation of CO<sub>2</sub> to form methane (CH<sub>4</sub>) has spurred an interest among researchers worldwide advocating the power-to-gas technology [2–6], as it can be used for chemical energy storage as well as directly pumped into the existing gas lines without major modifications. Further, it has recently been viewed as a plausible candidate for space applications [6]. The catalytic hydrogenation is based on the Sabatier reaction,  $CO_2 + 4 H_2 \rightleftharpoons CH_4 + 2H_2O$ ;  $\Delta H^0 = 165 \text{ kJ mol}^{-1}$ , which requires 4 moles of hydrogen which can be obtained from renewable sources, such as converting excess electricity to hydrogen from catalytic water splitting and biomass gasification [7–9].

Metal-metal oxides (M-M<sub>x</sub>O<sub>y</sub>) based systems have been inherently utilised to tackle the issue of methanation of CO<sub>2</sub> because of their superior mechanical performance and high stability. The most common active metals being Ni [10–17], Fe [18–20], Co [21–24] whereas the most common metal oxides supports are Al<sub>2</sub>O<sub>3</sub> [12–14,21,24–27], SiO<sub>2</sub> [28–30], ZrO<sub>2</sub> [10,31–33], CeO<sub>2</sub> [11,26,34–36] etc. Some noble metals like Ru [25,37–40] and Rh [41–43] provide better activity but are costly and susceptible to deactivation. The primary disadvantage of such systems is the ease of sintering of the metal nanoparticles (NPs) across the metal oxide supports because of lack of intrinsic M-M<sub>x</sub>O<sub>y</sub> interactions. Muroyama et. al. have reported the order of influence M-M<sub>x</sub>O<sub>y</sub> interactions according to the CH<sub>4</sub> yield at 250°C as Ni/Y<sub>2</sub>O<sub>3</sub> > Ni/Sm<sub>2</sub>O<sub>3</sub> > Ni/ZrO<sub>2</sub> > Ni/CeO<sub>2</sub> > Ni/Al<sub>2</sub>O<sub>3</sub> > Ni/La<sub>2</sub>O<sub>3</sub> [44]. It is regularly reported to be utilised in oxide based supports as they provide structural support necessary for high efficiency and recyclability, but is not ideal due to structural issues such as formation of spinel structures during calcination of Al<sub>2</sub>O<sub>3</sub> supports [45]. Recently, Ni has also been used along with promoters like Co [21], La [46] and Mn [47,48] to obtain CO<sub>2</sub> conversions of 65-82% with selectivity ranging from 84-99 %. The (111) facet of Ni has proved to be beneficial for CO<sub>2</sub> methanation over metal-organic framework substrates [49]. But, few studies have been carried out to utilise metal-non-metal oxide(M<sub>x</sub>-NM<sub>y</sub>) based catalysts for CO<sub>2</sub> hydrogenation, and even lesser reports involve carbon based nanomaterials for such reactions.

Carbon nanomaterials like nanotubes, nanofibers, graphene oxide and few-layer-graphene have been known to have unique properties which have shown promising results in the field of catalysis for energy applications [50]. The most common carbon structures studied for catalytic methanation of CO<sub>2</sub> have been carbon nanotubes [48,51] which provide the idea that there is still room for further investigations involving graphene and its derivatives. Graphene based derivatives needs to be studied as they can provide unique charge-transfer and heat transfer characteristics which can accelerate the catalytic processes. The π-electron charges clouding the basal plane of graphene makes it viable for anchoring of functional groups that can interact with excess electrons present on the oxygen atom of the CO<sub>2</sub> species which in turn acts as a self-promoting substrate. The extended π-orbital of graphene planes favour its interaction with the d-orbitals of metal-support atoms increasing

their stability [52], while the defects and edges are known to be good sites for attachment and stabilisation of metallic species [53,54]. Graphene has been used as photocatalyst with Ni dopants for CO<sub>2</sub> reduction but lacks high quantum yield [55]. It has also been studied for gas-phase methanation reactions. Ana et. al. have reported a directly proportional relationship between conversion rate and temperature using MoS<sub>2</sub> platelets along with FLG [52], but substantial conversion of CO<sub>2</sub> for this system arrives at a temperature of around 600°C which is pretty high in comparison to M-M<sub>x</sub>O<sub>y</sub> systems. Feiyang et. al. have recently demonstrated that Ni/RGO support alone is not a suitable candidate and needs Ce as promoter to achieve a conversion greater than 80% [56]. In the family of carbon supported Ni NPs, the best performance of methanation without additional promoter has been obtained for Ni/N-CNT showing 81% conversion at 360°C with a selectivity of 98% [51], while the reaction mechanism has been rarely discussed.

The heating conditions required to carry out methanation have recently been of interest as many studies tend towards using cleaner methods where highly disperse temperature ramp could be generated in few minutes contrary to the traditional Joule Heating method. Research driven towards Induction Heating (IH) has been gaining momentum recently pertaining to its favourable characteristics which allows for a precise, cost-effective and repeatable high temperature ramp and cool down within a few minutes [57,58]. The laser pyrometer guided real-time temperature control of reactor beds for such IH setups makes it a promising candidate for future applications in heterogenous catalysis where isothermal conditions and instant temperature ramps are considered essential. It has been already put into use for methanation of CO<sub>2</sub> [59], but the type of catalyst and substrate used has been restrictive in terms of need for additional promoter and efficiency. Wang et. al. have initially used this technique to achieve 71% conversion at 320°C with a carbon felt support [60]. Recently, they have reported use of a composite having high Ni loading (~ 40%) on an alumina support which has been able to provide a low temperature methanation [61]. There are several avenues concerning the design of catalyst and its integration to magnetically induced setup that can be improved. Graphene having its unique heat transfer properties becomes a suitable candidate for using such inductive heating based method [62]. FLG is advantageous considering the fact that it has properties similar to graphene while crediting itself as a good substitute for substrate for magnetic induced heating setups. It can help avoid formation of hotspots thereby increasing the lifecycle of catalyst and its methanation efficiency.

Herein, we demonstrate the use of carbon nanofibers covered few-layer-graphene as a suitable new hybrid support of Ni NPs for CO<sub>2</sub> methanation via inductive-heating process. The grown “herringbone” type CNFs having large number of active edges sites provide enhanced stabilisation of Ni NPs to achieve high NPs’ dispersion, while the presence of FLG enhances thermal conductivity [63]. Additional acid treatment of the support is applied to increase the CNFs edges activity. The impact of the growth parameters of CNFs on their morphology and distribution on FLG followed by their consequent effect on the NPs dispersion and methanation has been investigated. Ni has a double

faceted role in the composite by contributing to the heating via induction process as well as acting as active site for methanation.

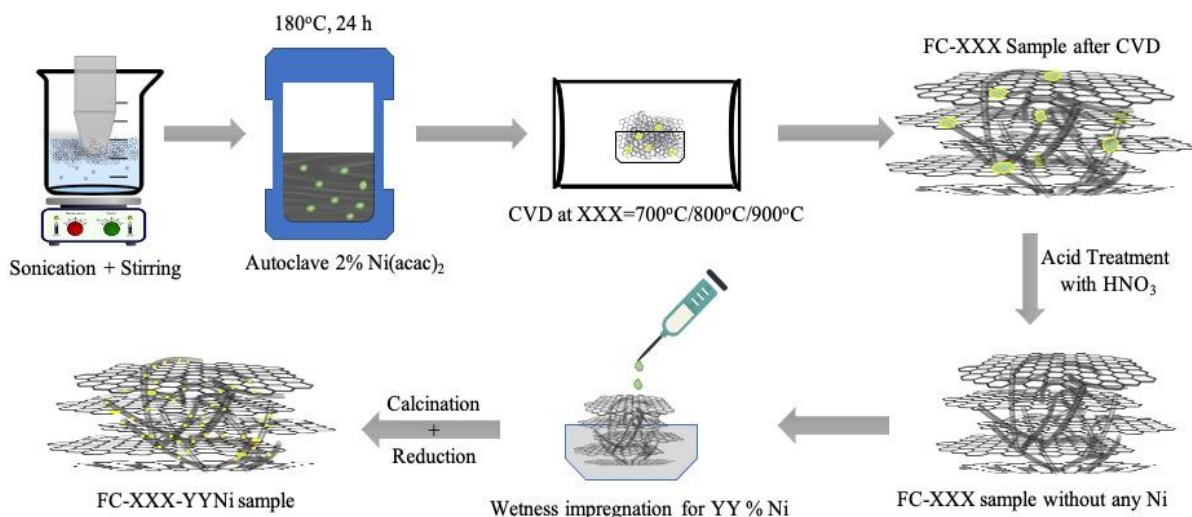
## **2. Experimental Section**

### **2.1 Synthesis of Carbon Nanofibers on FLG**

Expanded Graphite (EG) was purchased from Carbon Lorraine company, Bovine Serum Albumin(A) was purchased from Sigma Aldrich.  $\text{Ni}(\text{NO}_3)_2 \cdot 6\text{H}_2\text{O}$  and  $\text{Ni}(\text{acac})_2$  was obtained from Sigma Aldrich. Gases used for growth of CNFs was obtained from Air Liquide. The synthesis was carried out as shown in Erreur ! Source du renvoi introuvable.. The FLG was obtained similar to the previously reported work from the lab [63] with some modifications wherein EG is used in huge excess compared to the hHLB precursor. A typical synthesis involves dissolving about 600 mg of BSA (10% w/w of EG) in 500 ml ultra-pure water for 10 minutes followed by step-wise addition of 6gm of EG making sure it is properly wet and not coming out of the reaction beaker. Then the beaker is moved onto the stirring plus top-sonication setup which exfoliates the EG to FLG for about 2 hours at an amplitude of 25% power for the sonicator (BRANSON Sonifier 550) and stirring speed of 500-600 rpm. The solution was then centrifuged to remove major water content and obtain a paste like consistency of the FLG/hHLB mixture.

The product obtained was then mixed with 2% Ni from  $\text{Ni}(\text{acac})_2$  precursor in an autoclave with 300ml EtOH:H<sub>2</sub>O mixture of ratio 1:2. The sealed autoclave was subjected to 180°C for 24 hours. The autoclave was cooled down under tap water followed by retrieval of product. The product obtained was washed 3 times in water followed by oven drying. After overnight drying, it was calcined at 400°C for 3 hours.

This 2% Ni-FLG composite was used for growth of carbon nanofibers (CNFs) by Chemical Vapour Deposition (CVD) process at 3 different temperatures, giving rise to FC-XXX samples where XXX is 700°C/ 800°C/ 900°C depending on the growth temperature. Initially, the composite was heated under Argon till 400°C. The hydrogen was the introduced with simultaneous argon cut-off. The oven remained at 400°C for 2 h to obtain maximum reduced Ni NPs which will be the active sites for CNF growth. After reduction, the temperature was increased up to the 3 different temperatures mentioned earlier by changing back to Ar atmosphere. At the target temperature, CNF was grown for 2 h under 1:1 mixture of ethane and hydrogen flowing at a combined rate of 65 ml min<sup>-1</sup>. After the growth time, the reaction mixture was replaced with Ar and the reactor was cooled to room temperature.



*Scheme 1 Representation of synthesis procedure for FC-XXX-YYNi samples*

## 2.2 Preparation of Final Catalyst

After the growth of CNFs, the product recovered was treated with nitric acid (35%) at 800°C for 24 h under reflux conditions for complete removal of Ni used for growth as shown in Erreur ! Source du renvoi introuvable.. The composite was washed multiple times with ultrapure water till the litmus gave a neutral pH. Then it was dried overnight following which Ni was introduced with different mass loadings of 10%, 20%, 40% compared to FLG-CNF weight giving rise to the FC-XXX-YY-Ni coding of the samples with ‘YY’ representing the percentage of mass loading. A Ni ethanol solution from  $(\text{NiNO}_3)_2 \cdot 6\text{H}_2\text{O}$  was added via wetness impregnation followed by overnight oven drying at 110°C. Next, it was calcined at 250°C for 2 h to get rid of all excessive moisture. Lastly, the sample was reduced at 350°C for 2 h under hydrogen before use in reactor. Such treatment should ensure decomposition and reduction of supported Ni [64,65]. Thus, the catalyst was ready for further analysis and prior to the tests they were re-reduced/stabilized at 350°C for 0.5-1h.

## 2.3 Characterisation

Scanning electron microscopy (SEM), Scanning transmission electron microscopy (STEM) and High-angle annular dark-field (HAADF) was conducted on a ZEISS Gemini SEM 500 microscope with a resolution of 5 nm. For each measurement, samples were dispersed in ethanol for a few minutes and were drop-casted onto copper grids. Transmission Electron Microscopy (TEM) was carried out on a JEOL 2100 F microscope working at 200 kV voltage with a point-to-point resolution of 0.2 nm. For TEM also, samples were previously dispersed in ethanol using ultrasonication (for few minutes) till a homogeneous dispersion is obtained and the resulting solution was drop-casted on a copper grid covered with a holey carbon membrane. Thermal gravimetric analysis (TGA) analysis was carried out in the 30-850 °C temperature range (heating rate of 5 °C min<sup>-1</sup>) using a TGA Q5000 instrument operating under an air flow (25 mL min<sup>-1</sup>). The Brunauer-Emmett-Teller (BET) specific surface areas

(SSA) and porosity were calculated from N<sub>2</sub> physisorption isotherms recorded at 77 K on an ASAP 2020 Micromeritics® instrument. Pore size distribution was determined by Barrett-Joyner-Halenda (BJH) method. XPS analyses were performed with a MULTILAB 2000 (THERMO) spectrometer equipped with Al K anode ( $h\nu = 1486.6$  eV). For deconvolution of spectra, the CASA XPS program with a Gaussian-Lorentzian mix function and Shirley background subtraction was employed. Powder X-ray Diffraction (PXRD) measurements were carried out on a Bruker D-8 Advance diffractometer equipped with a Vantec detector (Cu K $\alpha$  radiation) working at 40 kV and 40 mA. X-ray diffractograms were recorded in the 10-80°  $2\theta$  region at room temperature in air.

CO<sub>2</sub>-temperature programmed desorption (TPD) experiments were performed on a mass spectrometer (MS). Prior to CO<sub>2</sub>-TPD, 50 mg of catalyst was in situ reduced by H<sub>2</sub> flow (30 mL min<sup>-1</sup>) at 350 °C for 1 h. Then, the sample was cooled to room temperature with Ar and saturated by CO<sub>2</sub>. After flushing with Ar for 1 h, the sample was heated to 600 °C by ramping at 5 °C min<sup>-1</sup> in Ar flow. The detected signals for CO<sub>2</sub> was  $m/z = 44$ .

Temperature-programmed surface reaction (TPSR) experiment was carried out on a mass spectrometer using Ar as the carrier gas. The main detected signals for each gas were  $m/z = 44$  (CO<sub>2</sub>), 2 (H<sub>2</sub>), 28 (CO), 16 (CH<sub>4</sub>), and 40 (Ar). The flow rate was corrected to be 40, 4, and 1 mL min<sup>-1</sup> for Ar, H<sub>2</sub>, and CO<sub>2</sub>, respectively. Prior to the experiment, the catalyst was reduced by H<sub>2</sub> at 350 °C for 1 h. The temperature was cooled down to 150 °C and maintained for 1 h until the baseline was stable. The reaction mixture was introduced into the reactor and the evolution of gases were monitored until the temperature increased to 450 °C at a rate of 5 °C min<sup>-1</sup>.

## 2.4 Inductive Heating (IH) Setup

The induction heating setup (EasyHeat 8310, 10 kW, Ambrell Ltd) is made up of a spiral 6-turn induction coil (length = 1.05 m, pure coil resistance =  $2.066 \times 10^{-3}$   $\Omega$ ), cooled by means of an external chiller with recirculated water/glycerol (10%) mixture. The sample was initially placed inside a quartz reactor fabricated specifically considering the internal diameter of the coil. In a typical experiment, the quartz reactor was first placed inside the induction heater coils such that the catalyst held by quartz wool is placed midway of the induction coil. The temperature was controlled in real-time by a PID system (Proportional Integral Derivative controller, Eurotherm model 3504) connected to a laser pyrometer (Optris,  $\emptyset$  laser beam:  $\approx 500$   $\mu\text{m}$ , power  $< 1$  mW, located at  $\approx 30$  cm from the catalyst) directed to the catalyst bed and working in the 150-1000 °C range (accuracy  $\pm 1$  °C). The temperature ramp rate allowed for the system is 50-70 °C min<sup>-1</sup> in the 250-450 °C temperature range.

CO<sub>2</sub> methanation reaction was carried out at atmospheric pressure in a fixed bed quartz tubular reactor [ $\emptyset_{\text{internal}} = 12$  mm, length = 400 mm] loaded with 200 mg of FLG-CNF/Ni catalyst over quartz wool. The reactants and products for IH heating setup were analysed online by a CP-3800 gas chromatograph (GC) equipped with a thermal conductivity detector (TCD) and a flame ionization

(FID) detector. All reactor exit lines were maintained at 110 °C by external heating tapes so as to avoid condensation of residual water in the gaseous feedstock to the GC. Prior to the tests the samples were stabilized under H<sub>2</sub> for 0.5 h at 350°C.

## 2.5 Joule Heating Setup

Carbon dioxide methanation was conducted at atmospheric pressure in a fixed-bed down-flow reactor at 350°C. A thermocouple was inserted in the furnace to measure the pre-treatment and reaction temperatures *in-situ*. The reactor was heated in a tubular furnace monitored by a temperature controller.

The flow of reactants was regulated by calibrated mass flow controllers (Brooks). H<sub>2</sub> and CO<sub>2</sub> were mixed at a stoichiometric H<sub>2</sub>:CO<sub>2</sub> ratio of 4:1 and N<sub>2</sub> was added as an internal standard. The total flow rate was set to 55 mL min<sup>-1</sup> with catalyst charged (for e.g. 30 mg of FLG/C catalyst diluted with 300 mg of SiC) into the quartz tube reactor [ $\varnothing_{\text{internal}} = 6.5$  mm, length = 300 mm] corresponding to a gas hourly space velocity of around 60 000 h<sup>-1</sup>/ 180 000 h<sup>-1</sup>. The feed and products were analysed on-line by a micro gas chromatograph (INFICON-3000 Series Micro GC equipped with MS5A and PPQ columns). Prior to the tests the samples were stabilized under H<sub>2</sub> for 1 h at 350°C.

## 2.6 Catalytic Test Measurements

CO<sub>2</sub> conversion ( $X_{CO_2}$ ) and CH<sub>4</sub> selectivity ( $S_{CH_4}$ ) were calculated according to the following equations:

$$X_{CO_2}(\%) = \frac{F_{CO_2(inlet)} - F_{CO_2(outlet)}}{F_{CO_2(inlet)}} \times 100$$

$$S_{CH_4}(\%) = \frac{F_{CH_4(outlet)}}{F_{CO_2(inlet)} - F_{CO_2(outlet)}} \times 100$$

where,  $F_{CO_2(inlet)}$  &  $F_{CO_2(outlet)}$  represent the flow of CO<sub>2</sub> in the inlet and outlet respectively. Further,  $F_{CH_4(outlet)}$  refers to the flow of CH<sub>4</sub> obtained in the outlet.

## 2.7 Magnetic Hyperthermia and SAR Measurements

The SAR (W/g magnetic nanomaterial) were measured by using a calorimetric method with a DM 100 magnetic hyperthermia setup (applicator and controller, Nanoscale Biomagnetics™, nB) under the MaNIaC software. Vials adapted for SAR measurements were filled with 1.0 mL of each sample dispersed in toluene at 50 mg ml<sup>-1</sup> by sonication and then were submitted to alternating magnetic field at 796 kHz and 200 G (15.9 kA m<sup>-1</sup>). The temperature change was recorded for 150 s. A second order polynomial function allowed to fit the temperature profile and to determine  $[dT/df]_{t=0}$  as described by Perigo et al. [66] and in previous works [67,68] to evaluate the SAR value by using the following equation:

$$\text{SAR} = m_s \cdot \frac{C_s}{m_{\text{Ni/C}}} \cdot \left[ \frac{dT}{dt} \right]_{t=0}$$

where  $m_s$  and  $C_s$  are respectively the mass (kg) and the heat capacity ( $\text{J kg}^{-1} \text{K}^{-1}$ ) of the sample,  $m_{\text{Ni/C}}$  (g) is the mass of FLG-CNF-Ni material element present in the sample and  $(dT/dt)_{t=0}$  the derivative of the temperature at  $t = 0$  ( $\text{K s}^{-1}$ ).

### 3. Results & Discussion

Seven different key samples containing FLG, CNFs and Ni NPs in different ratios were synthesised according to Erreur ! Source du renvoi introuvable.. The CNFs were grown at 700, 800 and 900°C. The Ni loading was designed to be 10, 20 for all and additionally 40% for the carbon hybrid grown at 800°C. The catalysts have been denoted as FC-XXX-YY wherein XXX refers to the temperature of the growth of CNFs on FLG and YY refers to the percentage of Ni loading on the FLG-CNF composite. An additional remark of 'F' and 'S' is added to distinguish between fresh and spent catalyst correspondingly. Further, another set of samples without any loading recovered just after nitric acid treatment and washing are denoted as FC-XXX-NA (essentially the pure carbon supports before any metal loading).

### 3.1 Morphological and Physico-chemical Characterisation

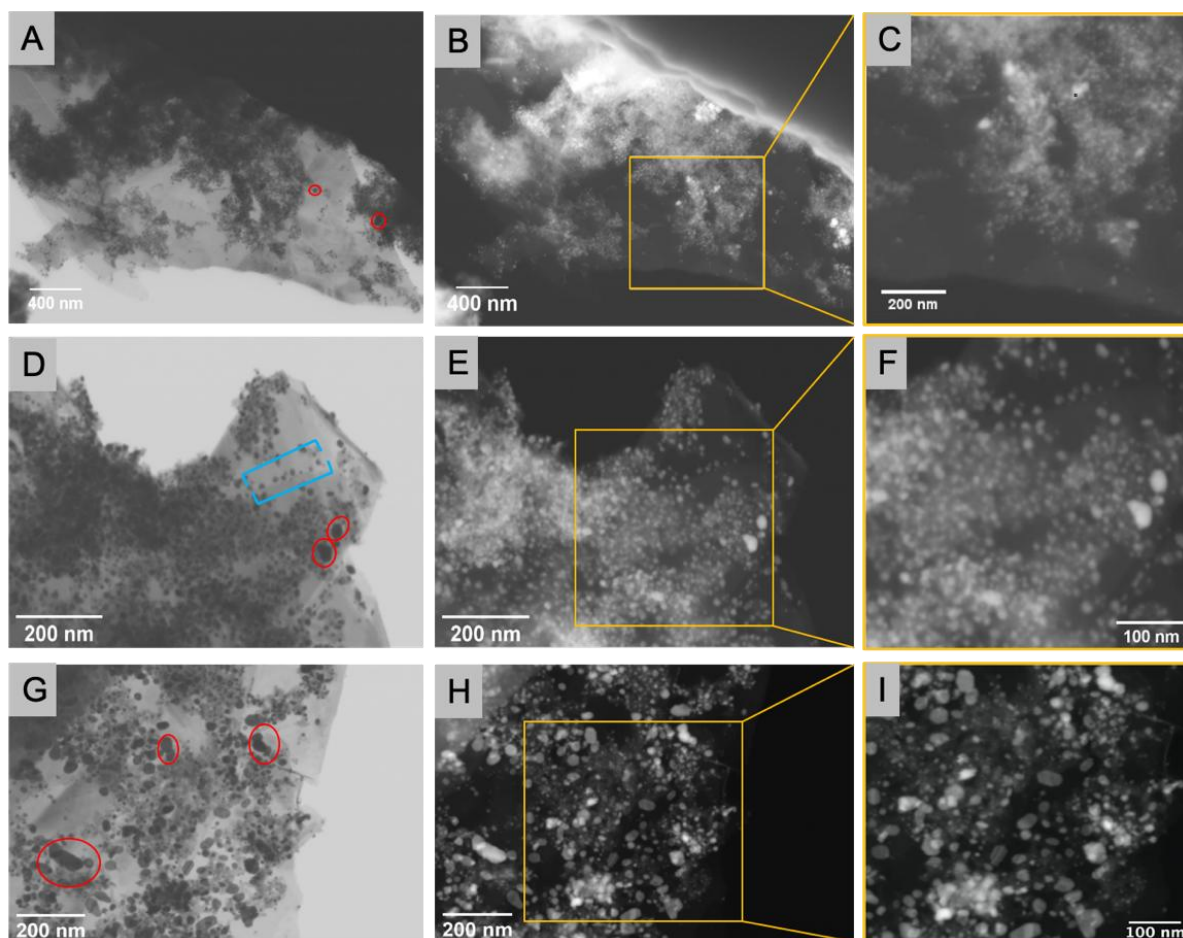


Figure 1 BF-STEM (1<sup>st</sup> column), HAADF-STEM (2<sup>nd</sup> column) and enlarged section (3<sup>rd</sup> column) of FC-800-10Ni (1<sup>st</sup> row), FC-800-20Ni (2<sup>nd</sup> row) and FC-800-40Ni (3<sup>rd</sup> row) respectively.

In order to understand the suitability of CNFs grown on FLG as a suitable support for Ni based CO<sub>2</sub> methanation in an inductive heating setup, the samples were characterised using SEM, TEM, TGA, XRD, N<sub>2</sub>- adsorption desorption. After synthesis, initially the samples were studied under the HR-SEM. **Figure 1** shows the STEM images of the FC-800 samples with various Ni loadings in each row. According to the HR-SEM and TEM observations, CNFs with herringbone attributed morphology has been found to be formed over the FLG flakes (**Figure SI 1.1 (a, b)**). Such CNFs have higher number of accessible edges which facilitate attachment and stabilization of active metal species. Multiple layers of graphene sheets forming FLG flakes tend to curl around each other with some wrinkles. The flakes seem to be tossed one above the other in a fashion that exposes their edges and partial surface every time. The Ni nanoparticles are mostly attached to the grown CNFs and edges of the FLG flakes (marked in blue in the images). Lesser amount has been found to be attached to the surface of the FLG sheets (**Figure SI 1.1 (c, d, e)**). There is a distinct rise in the size of Ni NPs and a gradual increase in agglomeration (marked in red in the images) of the same with the increase in amount of metal loading as can be seen from the high resolution images. A flattening of nanoparticles

to platelet forms along with agglomeration was observed for FC-800-40Ni sample having a high Ni loading of 40% (**Figure SI 1.2**) which is characteristic of high metal loadings on FLG [69].

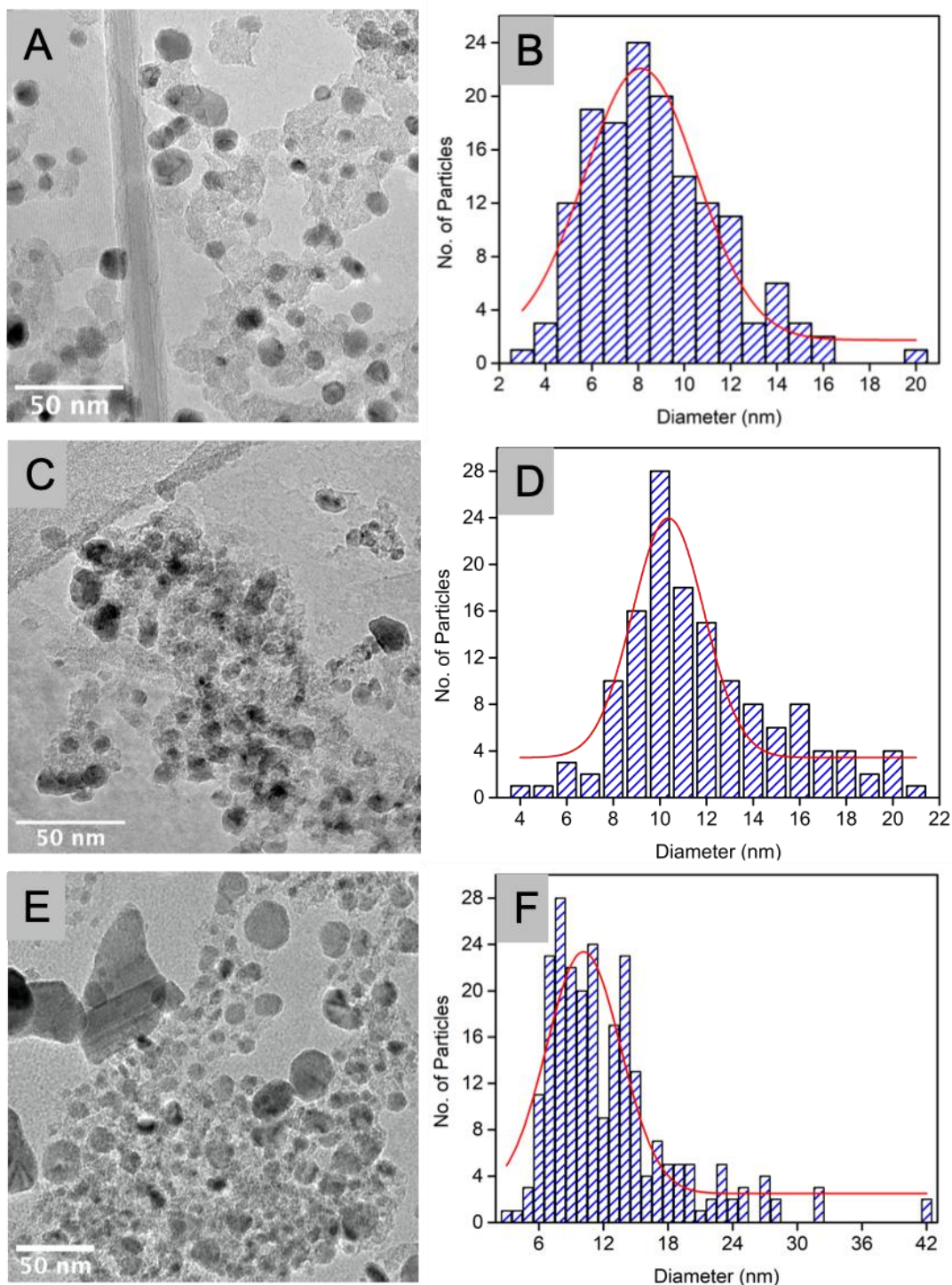


Figure 2 TEM images and Particle Size Distribution of FC-800-10Ni (a, b), C-800-20Ni (c, d), and FC-800-40Ni (e, f).

The samples were further studied with TEM microscopy in order to evaluate the particle size distribution as shown in **Figure 2**. The average particle size (obtained via Gaussian distribution of >100 NPs as sample set) for FC-800-10Ni was found to be ca. 8 nm, and that for the FC-800-20Ni

and FC-800-40Ni was found to be ca. 10 nm. FC-800-10Ni sample has however most of the Ni NPs in the range of 5-10 nm whereas FC-800-20Ni has most of the NPs in the range of 8-13 nm. It is interesting to note that although FC-800-40Ni has an average particle size of Ni NPs of ca. 11nm, a larger amount of the particles are more than 13 nm with some even higher than 30 nm. Further investigations revealed that the Ni NPs on FC-800-40Ni tend to stabilize to a larger extent along the edges of the FLG flakes (**Figure SI 1.3**) forming Ni NPs distinctively bigger than those attached to CNFs edges. This proves that with increase in the Ni loading on the supports, the particle size also increases. The increased size is typically detrimental for methanation reaction because the conversion depends on the amount of accessible active sites. Further, in **Figure 2 (a)**, a small amount of large particles can be seen which are mostly attached to the FLG edges as discussed earlier. It is noteworthy that with the increase in Ni loading, the particle size distribution sees not only a shift towards larger value, but also a more pronounced increase in the edge attachments can be seen as the population of NPs greater than 16 nm increases.

<i>Sample</i>	<i>Amount of Ni (%)<sup>a</sup></i>	<i>Size of Ni NPs<sup>b</sup></i>	<i>T<sub>max</sub> -IH (°C)</i>	<i>C/O ratio<sup>c</sup></i>
FC-800-10Ni-F	9	5-10 nm	>420	20
FC-800-20Ni-F	22	8-13 nm	>420	17
FC-800-40Ni-F	43	8-15 nm	>420	11
FC-700-10Ni-F	12	6-9 nm	>420	21
FC-700-20Ni-F	23	-	270	19
FC-900-10Ni-F	10	6-10 nm	>420	23
FC-900-20Ni-F	21	-	320	22

*Table 1 List of samples with their chemical composition and average particle size. \*a- obtained from TGA; \*b- Average diameter obtained from TEM analysis; \*c- Obtained from XPS (have approximative character)*

**Table 1** comprehensively identifies the chemical composition of the samples and average particle size of the Ni NPs present on the FLG-CNFs (FC) composite. TGA studies revealed that the actual Ni weight present in the catalyst after all treatments is not exactly equivalent but very close to the theoretical approximation used during the incipient wetness impregnation method. The TGA and DTG curves for the set of samples prepared at 800°C are presented in **Figure SI 1.4**, which reaffirms the fact that deposition of Ni in the FC-800-NA samples reduces their combustion temperature based on the type of carbon Ni is attached to. The two distinctly observed slopes arise from the two different types of carbon present in the composites. It can be considered that the CNFs are burnt faster than the graphene flakes since the amount of edges in CNFs which aid combustion is much higher than the C=C planes contrary to the large flakes of FLG. Further, composite localizations having higher amount of Ni gives rise to higher presence of Ni oxides, thus confirming that CNFs will burn faster than FLG because of higher Ni attachments.

An important aspect of the materials was understood by heating them under Argon in the IH setup. It was found that not all the samples can be heated to the reaction temperature in this set-up contrary to that in the Joule Heating setup. All the FC-800 derived samples were easy to heat to 420°C and beyond whereas the samples from FC-700 and FC-900 had issues with higher Ni loading. Both systems had good heating with a 10% Ni doping but failed to heat after a certain extent when loaded with 20% Ni owing to limitations of power supply. This is supposedly due to their differences in the interactions dominated by the structure of the supports and metal dispersions which is explained in detail later (**3.7 Role of Support Structure**).

An insight into the elemental composition were obtained by XPS studies of the composites (**Table 1** and **Table SI 1.1**). The various types of carbon bonding were approximated based on the deconvolution of XPS C1s spectra. XPS being a local measurement and the samples being readily oxidised render a close resemblance of C1s peaks and percentage of different kind of bondings for all samples. For this reason, the C/O ratios and the  $sp^2$  carbon values presented in the table have an approximative character. A deconvoluted C1s spectra shown in **Figure SI 1.5 (a)** indicates a typical carbon peak for graphene the materials with a large percentage of  $sp^2$  carbon. The two different types of carbon present in the sample makes it difficult for a proper estimation. The Ni 2p spectra for all samples follow the same order as FC-800 samples shown in **Figure SI 1.5 (b)**. The increase in Ni loading increases the intensity but the peak formation remains constant.

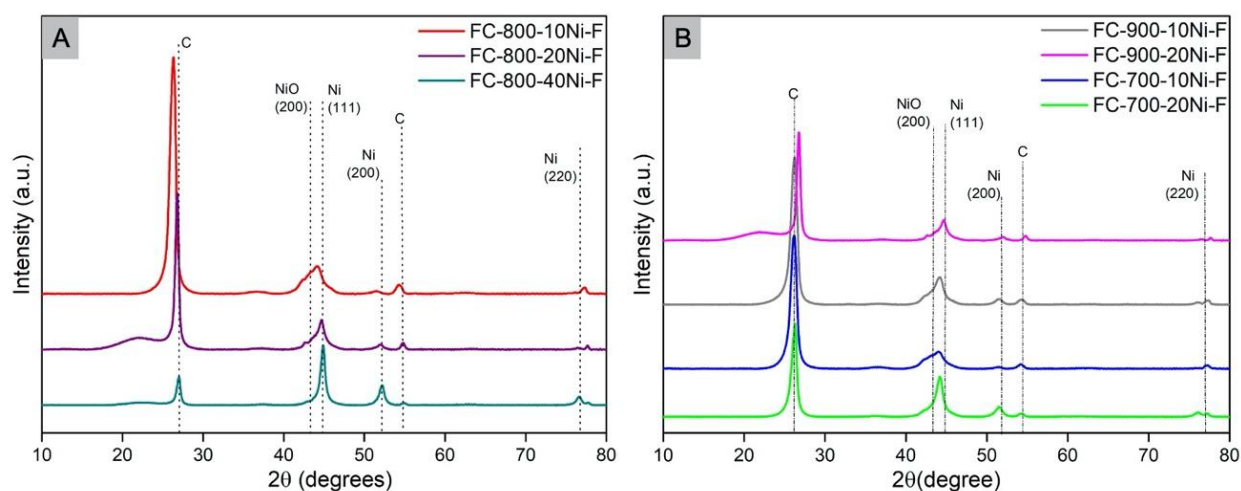


Figure 3 XRD spectra of, (a) FC-800-YY, (b) FC-700-YY & FC-900-YY.

The XRD patterns obtained for the composites were in agreement to that studied in literature [70,71]. The diffraction peaks at  $2\theta = 26.6^\circ$ ,  $54.8^\circ$  corresponded to carbon peaks arising from the FLG/C supports. In particular, characteristic FLG, metallic Ni and NiO peaks can be seen for all samples in **Figure 3**. The face centred cubic (fcc) Ni peaks were observed at  $44.8^\circ$  (111),  $52.2^\circ$  (200), and  $76.8^\circ$  (220) (JCPDS card no.: 04-0850), whereas distinct NiO peaks were also visible at  $43.2^\circ$  (200) (JCPDS card no.: 44-1159) because of inherent oxidation reaction taking place when the samples were exposed to atmospheric air. The increase in the Ni content in FC-800-20Ni-F and FC-

800-40Ni-F is evident from the relative increase in height of the combined Ni and NiO peaks in comparison to the sharp FLG peaks for these samples. The sharp signal of metallic Ni in the FC-800-40Ni-F is attributed to the fact that larger Ni loading causes an agglomeration of Ni nanoparticles thereby allowing a larger amount of metallic Ni remain unoxidized. This is also in tandem to the particle size obtained via TEM. The oxidized Ni phase is probably absent in the catalytic set-ups, where additional reduction/stabilization step at 350°C is applied prior to the methanation reaction. Since the investigation of reduction kinetics for Ni supported over nanocarbons are scarce in literature, we know that the reduction at 350°C of Ni supported on oxides such as Al<sub>2</sub>O<sub>3</sub> allow to get metallic Ni active phase, while interfacial, stabilizing oxide layers do not take a part in the catalytic process [72].

Sample	S <sub>BET</sub> [m <sup>2</sup> g <sup>-1</sup> ] <sup>a</sup>	V <sub>p</sub> [cm <sup>3</sup> g <sup>-1</sup> ] <sup>b</sup>	d <sub>p</sub> [nm] <sup>c</sup>
<b>FC-800-AAC</b>	37	0.12	13
<b>FC-800-NA</b>	179	0.55	13.4
<b>FC-800-10Ni-F</b>	172	0.42	11
<b>FC-800-20Ni-F</b>	147	0.33	10
<b>FC-800-40Ni-F</b>	107	0.25	10.4
<b>FC-900-10Ni-F</b>	54	0.14	12
<b>FC-900-20Ni-F</b>	48	0.14	10.3
<b>FC-700-10Ni-F</b>	160	0.3	7.5
<b>FC-700-20Ni-F</b>	128	0.25	7.4

*Table 2 Table showing surface properties of various FC samples. \*a- Specific surface areas calculated from the BET equation, \*b- Mesopore volumes obtained from the BJH desorption calculation method, \*c- Average pore width from the BJH desorption calculation method.*

BET surface area measurements (as shown in **Table 2**) reveal that the growth of nanofibers improves the surface area of the FLG composites largely. The multi-fold increase in surface area from 37 m<sup>2</sup> g<sup>-1</sup> of FC-800-AAC (sample after auto clave) to 179 m<sup>2</sup> g<sup>-1</sup> FC-800-NA (after growth of CNFs followed by nitric acid treatment) indicates that the introduction of CNFs onto the FLG flakes enhances its surface area and porosity. Such low surface area of the FC-800-AAC sample is also be attributed to the interlayer  $\pi$ - $\pi$  restacking increased during the long degassing process before the chemisorption studies and also due to inherent tendency of FLG flakes of 7-9 layers. All the samples tend to follow Type IV isotherms with a one-step capillary condensation typical of Ni supported composites (**Figure SI 1.6**) [73]. The increase in metal loading leads to a decrease in porosity (especially mesopores of c.a. 30-35nm) which is indicative of the pore blocking effect caused by the

Ni NPs. The size and amount of CNFs grown on the FLG seem to have a dominating effect on the  $S_{\text{BET}}$  as composites with same Ni loading tend to have distinctly different surface areas.  $S_{\text{BET}}$  clearly decreases with increase in % of Ni loading in the samples. Likewise, the  $S_{\text{BET}}$  also decreases with increase in diameter of CNFs.

### 3.2 CO<sub>2</sub>-TPD Measurements

The basicity and CO<sub>2</sub> adsorption capacity of FLG-CNFs samples were studied according to their CO<sub>2</sub>-TPD profiles as shown in **Figure 4**. For all catalysts, no physisorbed and weaker chemisorbed CO<sub>2</sub> basic sites were observed as no desorption occurred below 300°C. Most of them indicated presence of moderate basic sites indicated by the peaks in between 380-470°C. The FC-800 samples desorb at a lesser temperature compared to FC-700 and FC-900 samples which makes it a better candidate for CO<sub>2</sub> methanation. The CO<sub>2</sub> desorption curves for the support sample (FC-900-NA) presented in **Figure SI 1.7** suggests that both support has minor contribution in CO<sub>2</sub> adsorption for formation of reaction intermediate which results in methanation. Thus metal NPs are the most active sites for such catalysts.

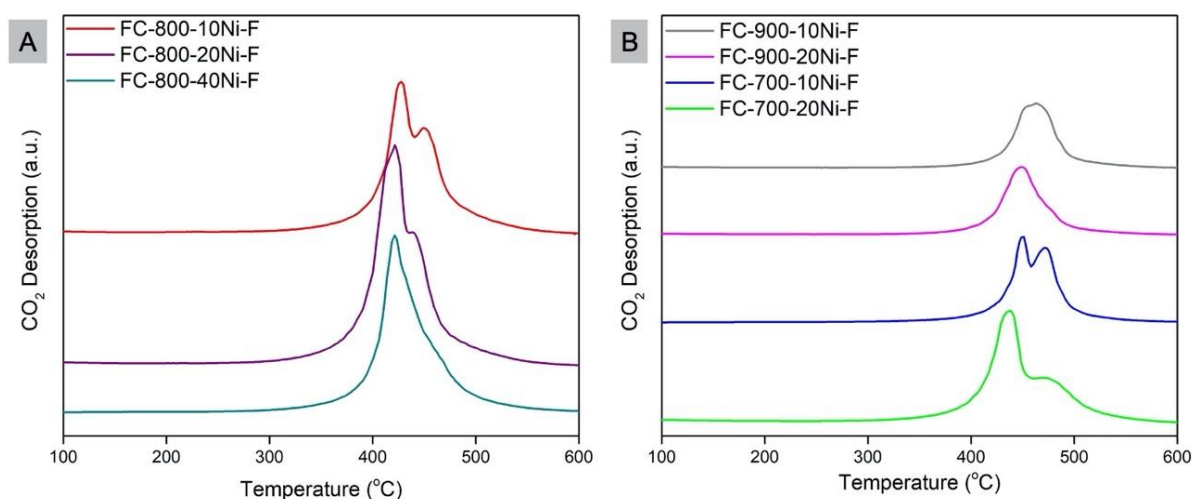


Figure 4 CO<sub>2</sub>-TPD profiles of FLG-CNFs composites.

### 3.3 Catalytic Activity

The performances of the catalysts were measured at 280-420°C temperature range by quantifying the CO<sub>2</sub> conversion ( $X_{\text{CO}_2}$ ) and CH<sub>4</sub> selectivity ( $S_{\text{CH}_4}$ ) as can be seen from **Figure 5**. It must be noted that, in all the cases, CO was not detected by the GC-MS at all temperatures. For all the samples, the FLG-CNFs support synthesized at different temperatures were first heated under regular reaction conditions in the induction heating setup without any Ni loading in order to confirm the negligible/null activity of the carbon support in absence of Ni. This ensured that all of the conversion obtained after loading arises due to the metal NPs. As a general trend, it can be noticed that the rate of  $X_{\text{CO}_2}$  increased with increasing temperature till 360°C for most samples indicating that the reaction is under

thermodynamic control in this regime optimising for stable product [74,75]. This effect is more pronounced for the FC-800 samples whereas the maximum  $X_{CO_2}$  for FC-700-10Ni and FC-900-10Ni samples were observed at 400°C and 340°C respectively. As the loading is similar to that of FC-800-10Ni, it is imperative that such shift in conversion arises from the structural incoherencies of the samples.

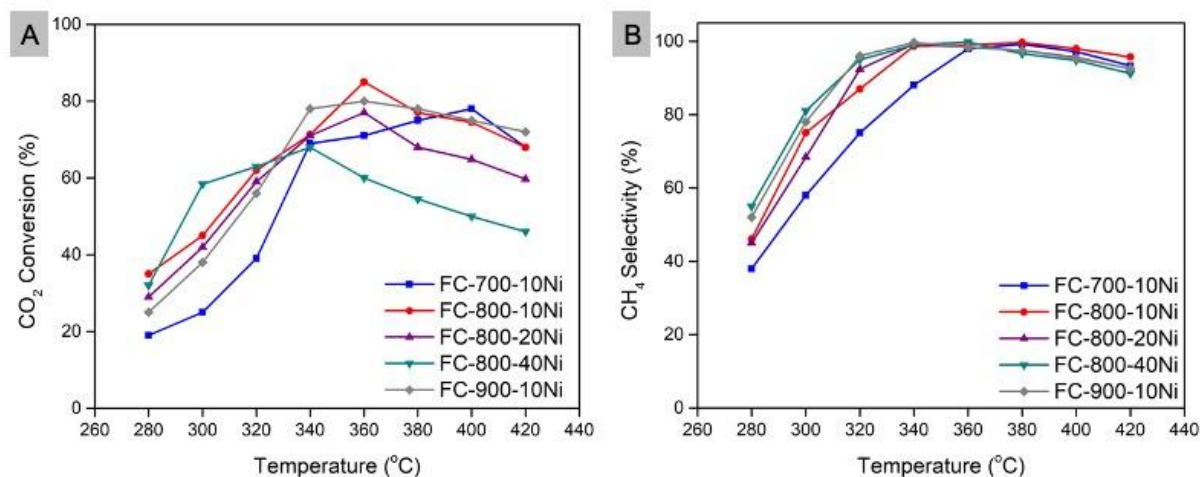


Figure 5 Conversion and Selectivity of  $CO_2$  and  $CH_4$  respectively on FC samples.

Comparing the conversion at the lowest feasible temperature under GHSV of  $30,000 \text{ ml g}_{\text{cat}}^{-1} \text{ h}^{-1}$  constituting of pure reaction gas mixtures only without any adulteration of inert gas, FC-800-10Ni-F seems to be significantly superior with an 85%  $CO_2$  conversion and 99.6%  $CH_4$  selectivity at 360°C. This proves that FLG as a support having a very good thermal conductivity is able to avoid formation of local heat gradients which is common in methanation reactions even at low GHSV with inert gas mixtures [76]. The decrease in gradient of both  $X_{CO_2}$  and  $S_{CH_4}$  after these temperatures is common for methanation with such carbon based supports [51,60] and can be attributed to the occurrence of overpowering parallel reactions like water-gas shift reaction, reverse water-gas shift reaction or steam reforming reaction [77] which are favoured at higher temperatures. Water gas shift reaction causes decrease in  $X_{CO_2}$  whereas both reverse water-gas shift reaction and steam reforming reaction cause decrease in  $S_{CH_4}$ . It is noteworthy that with such FC support materials,  $X_{CO_2}$  decreases with the increase in Ni loading which can be attributed to the increase in the Ni NPs size. The increase in the particle size reduces the effective active surface area of the catalyst for reaction to occur. The FC-700 and FC-900 samples on the other hand showed reasonable amount of  $X_{CO_2}$  with 10% Ni loading but faced issues via inductive heating when the loading was increased to 20%. As discussed earlier, we claim that this is because of the agglomeration of Ni NPs on CNF and FLG and their modified interaction with the FLG-CNF support structure causing anisotropic heat conduction and thereby limiting the temperature the sample can obtain for the same applied power.

### 3.4 Effect of Reaction Gas Ratio and GHSV

In order to better understand the  $X_{CO_2}$  capabilities of the best sample identified earlier, i.e. FC-800-10Ni, tests were carried out under various conditions mimicking the idea of dynamic nature in upscaled industrial plants. The  $X_{CO_2}$  and  $S_{CH_4}$  was measured in a reaction mixture having a stoichiometric excess of hydrogen which makes it more favourable for methanation. An increase in  $H_2$  indeed resulted an increase in  $X_{CO_2}$  up to a maximum of 96.8% with an  $S_{CH_4}$  of 99.8% as shown in **Figure 6 (a)**. All the tests with various  $H_2$  to  $CO_2$  ratios and different temperatures were carried out on the same sample with changing temperature and gas inflow as and when required. Such rapid change of heat is possible only in case of an inductive heating setup where temperature gradient can be neutralised at an approximate rate of more than  $150^\circ C \text{ min}^{-1}$ . The adaptability of the FC-800-10Ni catalyst to such dynamic stat/stop cycles with changing gas mixture and temperature, providing similar  $X_{CO_2}$  at the end indicates the stability of such composite material to adverse conditions. This also confirms that FLG as a support having a very good thermal conductivity can be used in stress conditions without formation of local heat gradients and can provide a better  $CH_4$  output when hydrogen is provided in stoichiometric excess.

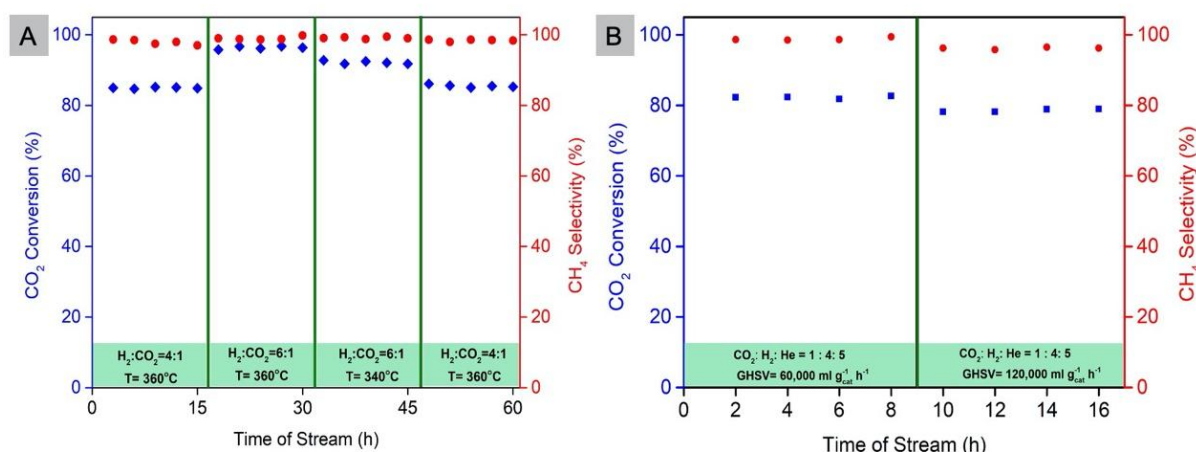


Figure 6 FC-800-10Ni sample under, (a) different reaction mixture ratio and temperature, (b) under different GHSV (blue dot- conversion, red dot- selectivity for the same sampling).

The validation of the catalyst stability to adverse conditions were further done by subjecting the FC-800-10Ni sample to gas flows having twice the GHSV or by reducing the mass of catalyst used initially. To make up for the high GHSV, equal amounts of reaction mixture and an inert gas like He was used as shown in **Figure 6 (b)**. It was found that  $X_{CO_2}$  decreased by 3% and 8% for  $60,000 \text{ ml g}_{\text{cat}}^{-1} \text{ h}^{-1}$  and  $120,000 \text{ ml g}_{\text{cat}}^{-1} \text{ h}^{-1}$  GHSV respectively. A lesser loss in  $S_{CH_4}$  was observed though for the same experiment with the lowest being  $\sim 95\%$  for GHSV of  $120,000 \text{ ml g}_{\text{cat}}^{-1} \text{ h}^{-1}$ . This further reassured the fact that a four times increase in GHSV does not decrease the efficiency of the catalyst to a larger extent.

### 3.5 Comparison with Joule Heating

The benefits of using an Inductive heating (IH) setup was understood by carrying out the same reaction in a conventional Joule heating (JH) setup. **Figure 7** shows the results of CO<sub>2</sub> methanation carried out with FC-800-10Ni catalyst under IH and JH setups at 60,000 ml g<sub>cat</sub><sup>-1</sup> h<sup>-1</sup> (108,000 h<sup>-1</sup>) and 60,000 h<sup>-1</sup> (33,333 ml g<sub>cat</sub><sup>-1</sup> h<sup>-1</sup>) GHSV respectively with a gas ratio maintained as CO<sub>2</sub>: H<sub>2</sub>: Inert gas (He/Ar) = 1: 4: 5. The test under JH was carried out up to 440°C where X<sub>CO<sub>2</sub></sub> achieved only 70%. It can be clearly seen from the two curves that the reaction takes off at a higher temperature in a JH setup compared to an IH setup. For example, a X<sub>CO<sub>2</sub></sub> of 61% and S<sub>CH<sub>4</sub></sub> of 98% can be achieved at 340°C in an IH (**Figure 7 (a)**) whereas similar results under a JH setup requires temperature as high as 400°C (**Figure 7 (b)**) The difference of 60°C for such conversion which prolongates further with increasing conversion proves the fact that IH is indeed a better approach for heating compared to JH for methanation reactions with samples at low metal NPs loading. This has a great industrial advantage as it has been already proven that a large amount energy for such reaction is used to heat the reaction unit rather than the catalyst itself [78]. Thus, IH not only facilitates tuning of the temperature and direct heating of catalyst but it also prevents loss of heat via convection and conduction from the reactor tube observed in case of JH. Further, the reduction temperature of the composite was also verified in order to make sure additional methane formation from the composite itself is not observed. Reduction at temperature of 450°C and beyond showed very minute but some C peaks on the micro-GC indicating decomposition of the composite which confirmed that 300-400°C working range is indeed most suitable for such composites.

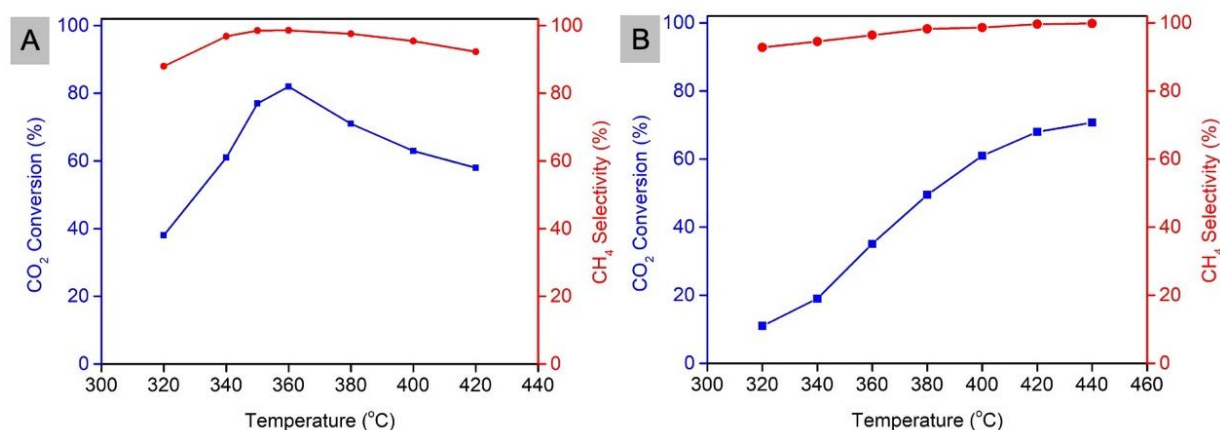


Figure 7 FC-800-10Ni CO<sub>2</sub> methanation under, (a) Inductive Heating at 60,000 ml g<sub>cat</sub><sup>-1</sup> h<sup>-1</sup> GHSV and, (b) Joule Heating at 60,000 h<sup>-1</sup> GHSV.

Temperature Programmed Surface Reaction (TPSR) studies being carried out in a manner analogous to the JH setup heats the entire sample chamber and sample as a whole and provides qualitative information concerning decomposition and formation of gas species as shown in **Figure 8**. TPSR studies revealed an interesting observation concerning the heating of the samples in two

different setups. It shows that JH is indeed helpful in case of samples like FC-700-20Ni and FC-900-20Ni which when tried in the IH setup could not be heated beyond a certain temperature owing to the limitations of the heating equipment which in turn depends on the structural properties and Ni NPs dispersion of the given composite. According to the TPSR analysis, the FC-700-20Ni-F catalyst seemed to be active and worthy for study in an IH setup. FC-700-20Ni under JH conditions showed a conversion of 67% at 440°C with almost 100% selectivity at a GHSV of 180,000 h<sup>-1</sup> which increases to a value of 73% when GHSV is decreased to 60,000 h<sup>-1</sup>.

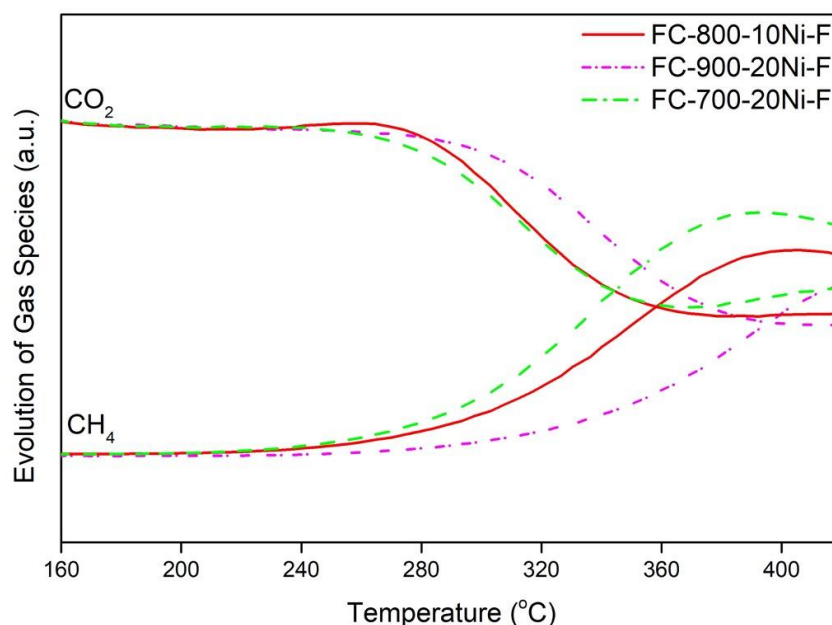


Figure 8 TPSR studies of some FLG-CNF samples.

### 3.6 Stability Tests

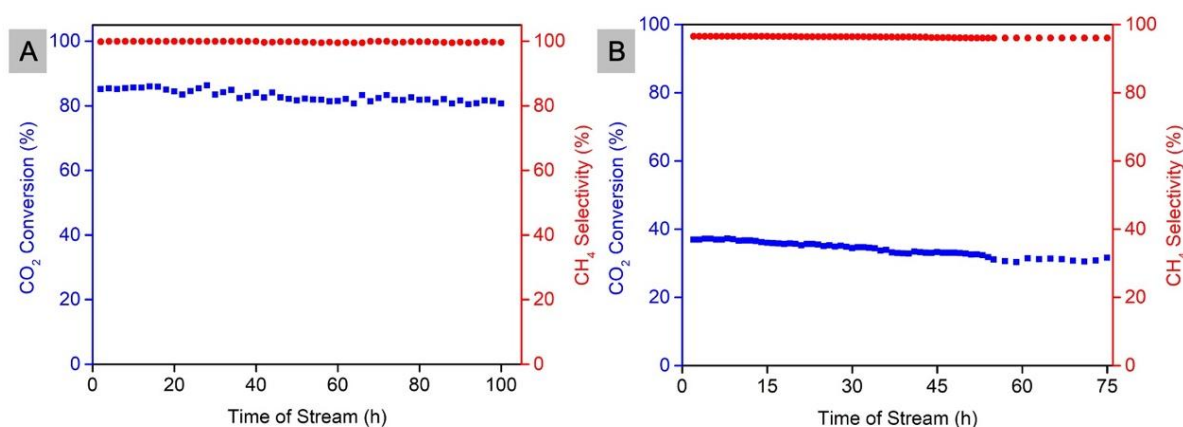
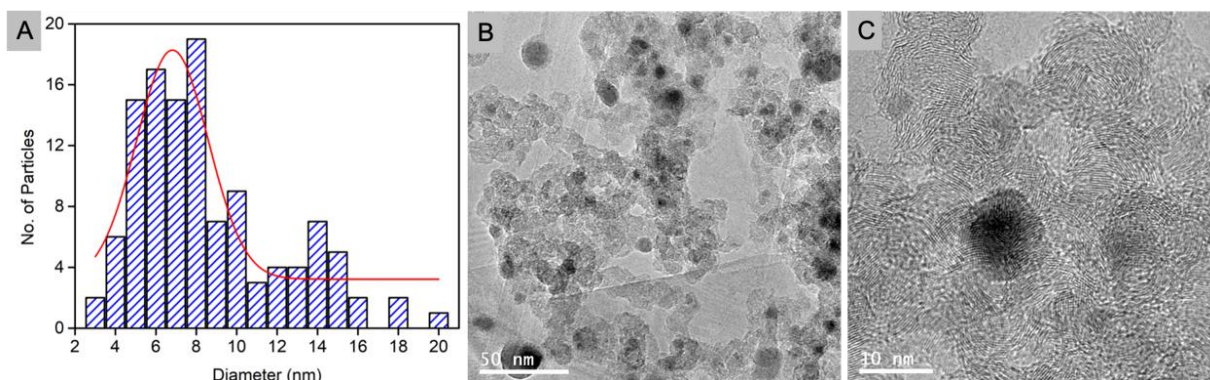


Figure 9 (a) Thermodynamic stability under IH and, (b) kinetic stability under JH for methanation with FC-800-10Ni sample.

A catalyst cannot be proposed for upscaling for industrial applications if the conversion is temporary or easily deactivated. In order to verify this, FC-800-10Ni sample was subjected to long

term stability tests under different conditions. Initially it was tested under the IH setup at 30,000 ml  $\text{g}_{\text{cat}}^{-1} \text{h}^{-1}$  GHSV under only  $\text{H}_2$  and  $\text{CO}_2$  gas mixture in stoichiometric ratios. After a test for 100 h as shown in **Figure 9 (a)**, it was found that the conversion has decreased by 4% with the selectivity remaining almost the same. This confirmed that the catalyst is able to perform the conversion in the desired form for a larger timeframe without any significant deactivation by processes like coke formation on active sites, sintering of metal nanoparticle or metal leaching. Sintering of Ni NPs due to formation of local temperature gradients in conventional setups has been confirmed by works of Wang [51] and Olesen [79]. Similarly, Salvatore et. al. have identified the formation of coke during methanation over Ni NPs is partially support dependent where-in the interaction of the Ni NPs with the support material govern their reactivity towards coke formation [80].

A similar test was carried out in the JH setup at 180000  $\text{h}^{-1}$  GHSV (**Figure 9 (b)**) contrary to the previous measurements at 60,000  $\text{h}^{-1}$  GHSV so as to better understand the kinetic product formation under more adverse conditions. A temperature of 360°C was chosen so as to avoid the thermodynamic equilibrium states where the majority product is methane. This test proved not only that the catalyst is stable in the JH setup for about 75h with a slight decrease of 5-6% in conversion but also proved that the selectivity stays high. It also confirmed that even at low conversion there was no CO product formation. We can find in literature that the lower selectivity observed in the IH setup can be attributed to the formation of other hydrocarbons at lower temperatures that are more kinetically favorable [81].



*Figure 10 Particle size distribution (a), and TEM micrographs (b, c) of FC-800-10Ni catalyst after stability test.*

A particle size analysis of the sample (**Figure 10 (a)**) retrieved after stability tests by TEM microscopy revealed that the majority of Ni NPs stay in the particle size range of 6-8 nm (**Figure 10 (b)**) similar to the ones before the test. Some of the particles in the image are larger than the rest which are mostly connected to the edges of the FLG flakes which has been a pronounced effect in all the samples. A strong interaction between the CNFs and the Ni NPs observed in **Figure 10 (c)** accounts for the high dispersity and avoidance of agglomeration after withstanding stability tests for 100 h. XPS surface analysis of the spent catalyst (**Figure SI 1.8**) further confirms absence of Ni-carbide species. Also, according to the TEM analysis, the formation of coke is null or negligible.

The potential methanation of the carbon support was also checked with FC-800-10Ni via the test without CO<sub>2</sub> injection. We could observed a first very weak signature of CH<sub>4</sub> formation at 420°C, which is above the operating temperature regime of CO<sub>2</sub> methanation of our system.

### 3.7 Role of Support Structure

The current study deals with three unique batches of materials which were prepared to identify the best balance between FLG and CNF deposits which can be next doped with nickel for efficient CO<sub>2</sub> methanation. The herringbone shaped CNFs forming in a stacked manner parallel to the FLG surface confirms the flat morphology of the Ni NPs during growth. It can be noted that initially FC composites were prepared at three different temperatures to which multiple loading of Ni were done to understand the influence of CNF growth temperature on the dispersion and stability of active sites. The thermal conductivity of the FLG support is very essential for such inductive-heating setups which in-turn depends on the crystal anharmonicity of the FLG lattice and defect scattering between the layers [82]. It has been found that the thermal conductivity of FLG decreases with the increase in the number of layers, thereby traversing towards bulk graphite limit [83].

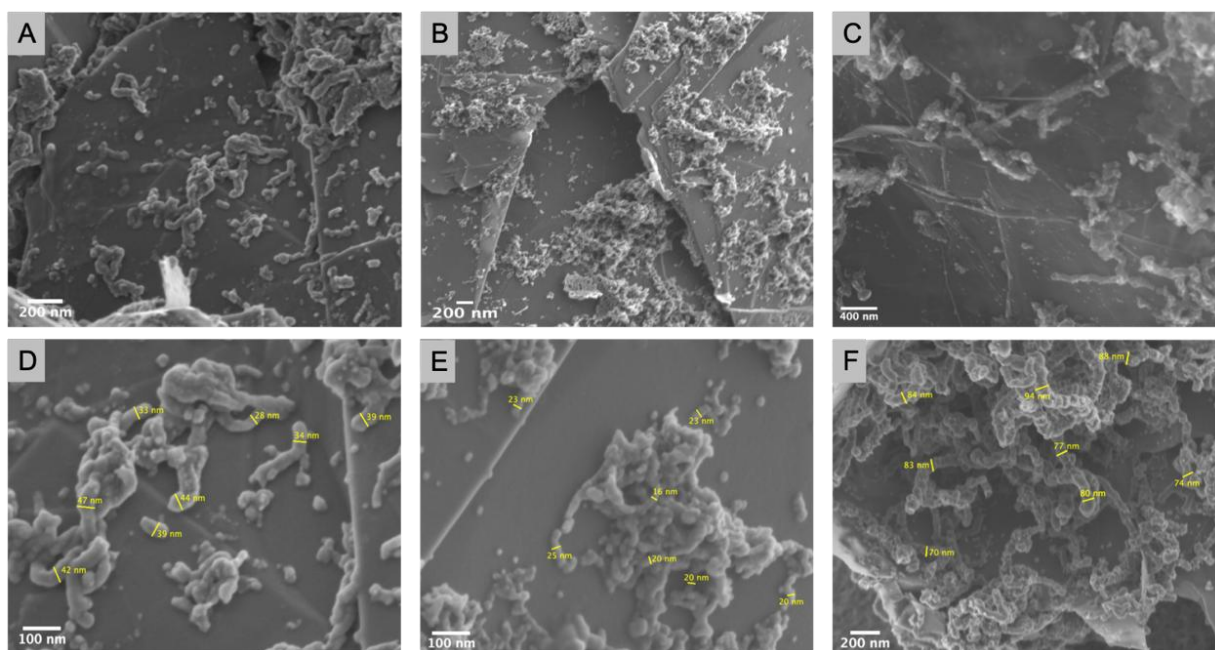


Figure 11 SEM images of FC-700(a,d), FC-800 (b,e), and FC-900 (c,f) samples indicating the CNFs distribution and diameter.

The FC-700 and FC-900 samples indeed have smaller surface area due to higher CNFs diameter compared to the 800°C sample. The improved surface area also confirms the avoidance of major re-stacking of FLG flakes. As seen in **Figure 11**, it is apparent that the thinnest CNFs are obtained at 800°C with a width less than 25 nm which is in tandem to its larger surface area in comparison to the samples prepared at 700°C and 900°C. The FC composites at 700°C have CNFs ranging from 30-50nm in diameter whereas the composites prepared at 900°C have CNFs ranging from 60-100nm.

With the multi-fold increase in the thickness of CNFs at 900°C it forms lesser amount of fibres in comparison to FC-800 and FC-700 samples where a large dispersed fibre cover is visible on the FLG flakes. This in-turn neutralizes the efficiency of the composite because the surface areas decreases (despite higher CNFs weight compared to those grown at 700°C and 800°C ) as well as makes favourable pathway for deposition of Ni on FLG flakes after CNFs edge saturation.

Sample	Amount of CNF(%)		Diameter of CNF <sup>b</sup> (nm)	T <sub>max</sub> – IH (°C)	C/O ratio <sup>c</sup>	% of sp <sup>2</sup> carbon <sup>c</sup>
	Weight	TGA <sup>a</sup>				
FC-700-NA	25	33	33-45	344	31	71
FC-800-NA	32	38	18-23	331	27	72
FC-900-NA	47	53	85-95	324	29	70

Table 3 Properties of FLG-CNF support materials. \*a- obtained from TGA; \*b- Average diameter obtained from SEM analysis; \*c- Obtained from XPS (have approximative character)

Additionally, as mentioned earlier, higher Ni loading makes larger aggregates causing inhomogeneous heating distribution. The heating limits for each support under IH setup is listed in **Table 3**. All support materials are able to heat and the similar temperature values could be detected with a difference of 10°C which is related probably to slightly different morphology, i.e. diameter of CNFs and consequently variable edges to plane ratio. The support materials have very close C/O ratio but still the lowest one is measured for FC-800-NA and the same tendency is confirmed in the composites with Ni, i.e. the amount of O increases with decrease of CNF diameter confirming higher oxygen sensitive edge content. Comparing FC-800-NA and FC-700-NA of similar weight, it can be seen that the ratio of edge-to-surface is higher in FC-800-NA attributed to lower diameter of CNFs in this sample, also confirmed by S<sub>BET</sub> (CNFs can be longer or higher in quantity). The optimum temperature of 800°C for the growth of CNFs over Ni NPs during the CVD process is probably a result of balance between lower coalescence of Ni NPs catalyst compared to 900°C and higher growing rate compared to 700°C. Since a direct effect of FLG-CNFs morphology on the heating capacity is very low, the IH heating in the composites with Ni is influenced by interactions of the support with Ni NPs and their morphology, distribution and amount of loading.

A study into the magnetic properties of the samples also confirmed that introduction of the Ni magnetic NPs onto the FLG-CNF composites increases its specific absorption rate (SAR, measured in toluene) with the FC-800 samples showing the maximum for a 10% loaded Ni sample (**Figure SI 1.9**, see temperature profiles). FC-800-10Ni indicates a SAR value of 8.16 W g<sup>-1</sup> (**Table SI 1.2**) which is distinctively more than all FC samples grown at various temperatures with 20% of Ni loading.

#### 4. Conclusion

A series of catalysts with varying diameter CNFs grown on FLG flakes subjected to impregnation with different loadings of Ni have been prepared. Further calcination and reduction steps rendered Ni NPs of diameter 6-8 nm or higher on the CNFs depending on the CNFs structure and size. Majority of the Ni NPs on FLG flakes were arranged along edges of carbon, *i.e.* edges of CNFs and also edges of FLG, with enhanced 2D aspects. A larger Ni loading gave rise to flattening of Ni NPs as platelets which further formed clusters. The samples were studied for their reactivity towards CO<sub>2</sub> methanation reaction in an Inductive heating setup which heats magnetically active catalyst. This mode of heating is found to be essentially beneficial in reducing the reaction temperature as well as to improving the efficiency. It also helps avoid the heat loss caused in reacting the entire reactor found in case of conventional Joule heating method. The CNFs grown at 800°C have shown the best reactivity with a loading of ~10% Nickel. The role of FLG-CNF support for methanation in IH Setup has been studied in detail which helps identify the key parameters for structure designing of supports. The 800°C grown CNFs had the lowest diameter in the range of 17-23 nm which allowed them for better dispersion of nanoparticles. The decrease in diameter goes with higher surface area and higher number of active sites (edges) to attach and stabilize NPs. More Ni NPs of lower dimension and higher dispersion is then obtained and thus higher efficiency. It was interesting to note that although FC-700-10 Ni and FC-700-20-Ni were prepared from the same batch of FLG-CNF composite, the 20% Ni loading maxed out the heating equipment but could not rise to a temperature suitable for methanation. Similar was the case for the FC-900 samples, although a high loading for FC-800 samples could be heated easily by the same setup. This indicates the fact that CNFs diameter beyond a certain limit when loaded with a larger amount Ni creates interaction and morphology which degrade its specific heat absorption capacities thereby making them unable to heat under same heating conditions. The reason for such behaviour can be studied further via magnetic properties analysis and specific absorption rate studies. Further, it was also proved that the Ni NPs dispersion on such supports stays stable for a long time in a thermodynamic regime and doesn't produce CO as by-product in a kinetic regime. To conclude, conversion of 85% with selectivity of 99.6% at a temperature of 360°C was achieved for the FC-800-10Ni sample in an Inductive Heating setup. Above this temperature, the drop of conversion and selectivity suggest presence of parallel reactions.

#### Author Contributions

Anurag Mohanty- Ideation, synthesis of materials, characterization of samples, catalytic measurements, writing of the manuscript.

Cuong Duong Viet – Initial operation of Inductive heating and GC-MS setup

Anne-Cecile Roger- Provide setup for Joule-heating and discussions for the same

Alexandre Adam- Carry out SAR experiments and formal analysis

Damien Mertz- Discussions related to SAR measurements and formal analysis

Walid Baaziz- Carry out TEM experiments and result discussion

Izabela Janowska- Ideation, supervision, validation, writing and editing of the manuscript.

### **Declaration of Competing Interest**

The authors declare that they have no known competing financial interests or personal relationships that could have appeared to influence the work reported in this paper.

### **Acknowledgements**

The authors want to acknowledge Fondation pour la Recherche en Chimie (FRC) for FRC-Solvay PhD fellowship of Dr. Anurag Mohanty. Dr. Cuong Pham-Huu and Dr. Wei Wang are acknowledged for providing set-up and help with the Induction Heating respectively. Dr. Jean-Mario Nhut is acknowledged for technical help concerned with the GC-MS. Anne-Clemence Aun is acknowledged for the help with Joule-heating setup. Dr. Vasiliki Papaefthimiou and Dr. Thierry Romero are acknowledged for performing XPS-measurements and carrying out SEM microscopy respectively.

## References

- [1] I. Tiseo, Historical carbon dioxide emissions from global fossil fuel combustion and industrial processes from 1758 to 2020, Statista. (2021).
- [2] A. Maroufmashat, M. Fowler, Transition of Future Energy System Infrastructure; through Power-to-Gas Pathways, *Energies* . 10 (2017). <https://doi.org/10.3390/en10081089>.
- [3] I. García–García, U. Izquierdo, V.L. Barrio, P.L. Arias, J.F. Cambra, Power-to-Gas: Storing surplus electrical energy. Study of Al<sub>2</sub>O<sub>3</sub> support modification, *Int. J. Hydrogen Energy*. 41 (2016) 19587–19594. <https://doi.org/10.1016/j.ijhydene.2016.04.010>.
- [4] A. Antenucci, G. Sansavini, Extensive CO<sub>2</sub> recycling in power systems via Power-to-Gas and network storage, *Renew. Sustain. Energy Rev.* 100 (2019) 33–43. <https://doi.org/10.1016/j.rser.2018.10.020>.
- [5] F.D. Meylan, F.P. Piguet, S. Erkman, Power-to-gas through CO<sub>2</sub> methanation: Assessment of the carbon balance regarding EU directives, *J. Energy Storage*. 11 (2017) 16–24. <https://doi.org/10.1016/j.est.2016.12.005>.
- [6] C. Vogt, M. Monai, G.J. Kramer, B.M. Weckhuysen, The renaissance of the Sabatier reaction and its applications on Earth and in space, *Nat. Catal.* 2 (2019) 188–197. <https://doi.org/10.1038/s41929-019-0244-4>.
- [7] R.M. Navarro, M.C. Sánchez-Sánchez, M.C. Alvarez-Galvan, F. Del Valle, J.L.G. Fierro, Hydrogen production from renewable sources: Biomass and photocatalytic opportunities, *Energy Environ. Sci.* 2 (2009) 35–54. <https://doi.org/10.1039/b808138g>.
- [8] I. Dincer, C. Acar, Review and evaluation of hydrogen production methods for better sustainability, *Int. J. Hydrogen Energy*. 40 (2014) 11094–11111. <https://doi.org/10.1016/j.ijhydene.2014.12.035>.
- [9] Z. Yan, J.L. Hitt, J.A. Turner, T.E. Mallouk, Renewable electricity storage using electrolysis, *Proc. Natl. Acad. Sci. U. S. A.* 117 (2020) 12558–12563. <https://doi.org/10.1073/pnas.1821686116>.
- [10] X. Jia, X. Zhang, N. Rui, X. Hu, C. jun Liu, Structural effect of Ni/ZrO<sub>2</sub> catalyst on CO<sub>2</sub> methanation with enhanced activity, *Appl. Catal. B Environ.* 244 (2019) 159–169. <https://doi.org/10.1016/j.apcatb.2018.11.024>.
- [11] R.P. Ye, Q. Li, W. Gong, T. Wang, J.J. Razink, L. Lin, Y.Y. Qin, Z. Zhou, H. Adidharma, J. Tang, A.G. Russell, M. Fan, Y.G. Yao, High-performance of nanostructured Ni/CeO<sub>2</sub> catalyst on CO<sub>2</sub> methanation, *Appl. Catal. B Environ.* 268 (2020) 118474. <https://doi.org/10.1016/j.apcatb.2019.118474>.
- [12] C. Italiano, J. Llorca, L. Pino, M. Ferraro, V. Antonucci, A. Vita, CO and CO<sub>2</sub> methanation over Ni catalysts supported on CeO<sub>2</sub>, Al<sub>2</sub>O<sub>3</sub> and Y<sub>2</sub>O<sub>3</sub> oxides, *Appl. Catal. B Environ.* 264 (2020) 118494. <https://doi.org/10.1016/j.apcatb.2019.118494>.

- [13] J. Lin, C. Ma, Q. Wang, Y. Xu, G. Ma, J. Wang, H. Wang, C. Dong, C. Zhang, M. Ding, Enhanced low-temperature performance of CO<sub>2</sub> methanation over mesoporous Ni/Al<sub>2</sub>O<sub>3</sub>-ZrO<sub>2</sub> catalysts, *Appl. Catal. B Environ.* 243 (2019) 262–272. <https://doi.org/10.1016/j.apcatb.2018.10.059>.
- [14] G. Garbarino, C. Wang, T. Cavattoni, E. Finocchio, P. Riani, M. Flytzani-Stephanopoulos, G. Busca, A study of Ni/La-Al<sub>2</sub>O<sub>3</sub> catalysts: A competitive system for CO<sub>2</sub> methanation, *Appl. Catal. B Environ.* 248 (2019) 286–297. <https://doi.org/10.1016/j.apcatb.2018.12.063>.
- [15] J. Wu, Z. Jin, B. Wang, Y. Han, Y. Xu, Z. Liang, Z. Wang, Nickel Nanoparticles Encapsulated in Microporous Graphenelike Carbon (Ni@MGC) as Catalysts for CO<sub>2</sub> Methanation, *Ind. Eng. Chem. Res.* (2019). <https://doi.org/10.1021/acs.iecr.9b03789>.
- [16] R. Zhou, N. Rui, Z. Fan, C. jun Liu, Effect of the structure of Ni/TiO<sub>2</sub> catalyst on CO<sub>2</sub> methanation, *Int. J. Hydrogen Energy.* 41 (2016) 22017–22025. <https://doi.org/10.1016/j.ijhydene.2016.08.093>.
- [17] C. Wang, P. Zhai, Z. Zhang, Y. Zhou, J. Zhang, H. Zhang, Z. Shi, R.P.S. Han, F. Huang, D. Ma, Nickel catalyst stabilization via graphene encapsulation for enhanced methanation reaction, *J. Catal.* 334 (2016) 42–51. <https://doi.org/10.1016/j.jcat.2015.10.004>.
- [18] J. Kirchner, J.K. Anolleck, H. Lösch, S. Kureti, Methanation of CO<sub>2</sub> on iron based catalysts, *Appl. Catal. B Environ.* 223 (2018) 47–59. <https://doi.org/10.1016/j.apcatb.2017.06.025>.
- [19] M.-D. Lee, J.-F. Lee, C.-S. Chang, Catalytic behavior and phase composition change of iron catalyst in hydrogenation of carbon dioxide., *J. Chem. Eng. JAPAN.* 23 (1990) 130–136. <https://doi.org/10.1252/jcej.23.130>.
- [20] Z. Baysal, S. Kureti, CO<sub>2</sub> methanation on Mg-promoted Fe catalysts, *Appl. Catal. B Environ.* 262 (2020) 118300. <https://doi.org/10.1016/j.apcatb.2019.118300>.
- [21] Q. Liu, B. Bian, J. Fan, J. Yang, Cobalt doped Ni based ordered mesoporous catalysts for CO<sub>2</sub> methanation with enhanced catalytic performance, *Int. J. Hydrogen Energy.* 43 (2018) 4893–4901. <https://doi.org/10.1016/j.ijhydene.2018.01.132>.
- [22] P. Riani, G. Garbarino, T. Cavattoni, F. Canepa, G. Busca, Unsupported cobalt nanoparticles as catalysts: Effect of preparation method on catalytic activity in CO<sub>2</sub> methanation and ethanol steam reforming, *Int. J. Hydrogen Energy.* 44 (2019) 27319–27328. <https://doi.org/10.1016/j.ijhydene.2019.08.228>.
- [23] J. Díez-Ramírez, P. Sánchez, V. Kyriakou, S. Zafeiratos, G.E. Marnellos, M. Konsolakis, F. Dorado, Effect of support nature on the cobalt-catalyzed CO<sub>2</sub> hydrogenation, *J. CO<sub>2</sub> Util.* 21 (2017) 562–571. <https://doi.org/10.1016/j.jcou.2017.08.019>.
- [24] T. Franken, J. Terreni, A. Borgschulte, A. Heel, Solid solutions in reductive environment – A case study on improved CO<sub>2</sub> hydrogenation to methane on cobalt based catalysts derived from ternary mixed metal oxides by modified reducibility, *J. Catal.* 382 (2020) 385–394. <https://doi.org/10.1016/j.jcat.2019.12.045>.

- [25] L. Falbo, C.G. Visconti, L. Lietti, J. Szanyi, The effect of CO on CO<sub>2</sub> methanation over Ru/Al<sub>2</sub>O<sub>3</sub> catalysts: a combined steady-state reactivity and transient DRIFT spectroscopy study, *Appl. Catal. B Environ.* 256 (2019) 117791. <https://doi.org/10.1016/j.apcatb.2019.117791>.
- [26] A. Cárdenas-Arenas, A. Quindimil, A. Davó-Quiñonero, E. Bailón-García, D. Lozano-Castelló, U. De-La-Torre, B. Pereda-Ayo, J.A. González-Marcos, J.R. González-Velasco, A. Bueno-López, Isotopic and in situ DRIFTS study of the CO<sub>2</sub> methanation mechanism using Ni/CeO<sub>2</sub> and Ni/Al<sub>2</sub>O<sub>3</sub> catalysts, *Appl. Catal. B Environ.* 265 (2020) 118538. <https://doi.org/10.1016/j.apcatb.2019.118538>.
- [27] B. Mutz, M. Belimov, W. Wang, P. Sprenger, M.A. Serrer, D. Wang, P. Pfeifer, W. Kleist, J.D. Grunwaldt, Potential of an alumina-supported Ni<sub>3</sub>Fe catalyst in the methanation of CO<sub>2</sub>: Impact of alloy formation on activity and stability, *ACS Catal.* 7 (2017) 6802–6814. <https://doi.org/10.1021/acscatal.7b01896>.
- [28] J.B. Branco, P.E. Brito, A.C. Ferreira, Methanation of CO<sub>2</sub> over nickel-lanthanide bimetallic oxides supported on silica, *Chem. Eng. J.* 380 (2020) 122465. <https://doi.org/10.1016/j.cej.2019.122465>.
- [29] Y.R. Dias, O.W. Perez-Lopez, Carbon dioxide methanation over Ni-Cu/SiO<sub>2</sub> catalysts, *Energy Convers. Manag.* 203 (2020) 112214. <https://doi.org/10.1016/j.enconman.2019.112214>.
- [30] G. Zhou, H. Liu, Y. Xing, S. Xu, H. Xie, K. Xiong, CO<sub>2</sub> hydrogenation to methane over mesoporous Co/SiO<sub>2</sub> catalysts: Effect of structure, *J. CO<sub>2</sub> Util.* 26 (2018) 221–229. <https://doi.org/10.1016/j.jcou.2018.04.023>.
- [31] W. Li, Y. Liu, M. Mu, F. Ding, Z. Liu, X. Guo, C. Song, Organic acid-assisted preparation of highly dispersed Co/ZrO<sub>2</sub> catalysts with superior activity for CO<sub>2</sub> methanation, *Appl. Catal. B Environ.* 254 (2019) 531–540. <https://doi.org/10.1016/j.apcatb.2019.05.028>.
- [32] J. Huang, W. Li, K. Wang, J. Huang, X. Liu, D. Fu, Q. Li, G. Zhan, M xO y-ZrO<sub>2</sub> (M = Zn, Co, Cu) Solid Solutions Derived from Schiff Base-Bridged UiO-66 Composites as High-Performance Catalysts for CO<sub>2</sub> Hydrogenation, *ACS Appl. Mater. Interfaces.* 11 (2019) 33263–33272. <https://doi.org/10.1021/acsami.9b11547>.
- [33] O.E. Everett, P.C. Zonetti, O.C. Alves, R.R. de Avillez, L.G. Appel, The role of oxygen vacancies in the CO<sub>2</sub> methanation employing Ni/ZrO<sub>2</sub> doped with Ca, *Int. J. Hydrogen Energy.* 45 (2020) 6352–6359. <https://doi.org/10.1016/j.ijhydene.2019.12.140>.
- [34] M. Li, H. Amari, A.C. van Veen, Metal-oxide interaction enhanced CO<sub>2</sub> activation in methanation over ceria supported nickel nanocrystallites, *Appl. Catal. B Environ.* 239 (2018) 27–35. <https://doi.org/10.1016/j.apcatb.2018.07.074>.
- [35] W.L. Vrijburg, J.W.A. Van Helden, A. Parastaev, E. Groeneveld, E.A. Pidko, E.J.M. Hensen, Ceria-zirconia encapsulated Ni nanoparticles for CO<sub>2</sub> methanation, *Catal. Sci. Technol.* 9 (2019) 5001–5010. <https://doi.org/10.1039/c9cy01428d>.

- [36] X. Guo, H. He, A. Traitangwong, M. Gong, V. Meeyoo, P. Li, C. Li, Z. Peng, S. Zhang, Ceria imparts superior low temperature activity to nickel catalysts for CO<sub>2</sub> methanation, *Catal. Sci. Technol.* 9 (2019) 5636–5650. <https://doi.org/10.1039/c9cy01186b>.
- [37] E. Truskiewicz, K. Kowalczyk, A. Dębska, D. Wojda, E. Iwanek, L. Kępiński, B. Mierzwa, Methanation of CO on Ru/graphitized-carbon catalysts: Effects of the preparation method and the carbon support structure, *Int. J. Hydrogen Energy.* 45 (2020) 31985–31999. <https://doi.org/10.1016/j.ijhydene.2020.08.235>.
- [38] A. Petala, P. Panagiotopoulou, Methanation of CO<sub>2</sub> over alkali-promoted Ru/TiO<sub>2</sub> catalysts: I. Effect of alkali additives on catalytic activity and selectivity, *Appl. Catal. B Environ.* 224 (2018) 919–927. <https://doi.org/10.1016/j.apcatb.2017.11.048>.
- [39] X. Wang, Y. Hong, H. Shi, J. Szanyi, Kinetic modeling and transient DRIFTS–MS studies of CO<sub>2</sub> methanation over Ru/Al<sub>2</sub>O<sub>3</sub> catalysts, *J. Catal.* 343 (2016) 185–195. <https://doi.org/10.1016/j.jcat.2016.02.001>.
- [40] F. Wang, S. He, H. Chen, B. Wang, L. Zheng, M. Wei, D.G. Evans, X. Duan, Active Site Dependent Reaction Mechanism over Ru/CeO<sub>2</sub> Catalyst toward CO<sub>2</sub> Methanation, *J. Am. Chem. Soc.* 138 (2016) 6298–6305. <https://doi.org/10.1021/jacs.6b02762>.
- [41] N.M. Martin, F. Hemmingsson, A. Schaefer, M. Ek, L.R. Merte, U. Hejral, J. Gustafson, M. Skoglundh, A.C. Dippel, O. Gutowski, M. Bauer, P.A. Carlsson, Structure-function relationship for CO<sub>2</sub> methanation over ceria supported Rh and Ni catalysts under atmospheric pressure conditions, *Catal. Sci. Technol.* 9 (2019) 1644–1653. <https://doi.org/10.1039/c8cy02097c>.
- [42] D. Heyl, U. Rodemerck, U. Bentrup, Mechanistic Study of Low-Temperature CO<sub>2</sub> Hydrogenation over Modified Rh/Al<sub>2</sub>O<sub>3</sub> Catalysts, *ACS Catal.* 6 (2016) 6275–6284. <https://doi.org/10.1021/acscatal.6b01295>.
- [43] A. Karelovic, P. Ruiz, Mechanistic study of low temperature CO<sub>2</sub> methanation over Rh/TiO<sub>2</sub> catalysts, *J. Catal.* 301 (2013) 141–153. <https://doi.org/10.1016/j.jcat.2013.02.009>.
- [44] H. Muroyama, Y. Tsuda, T. Asakoshi, H. Masitah, T. Okanishi, T. Matsui, K. Eguchi, Carbon dioxide methanation over Ni catalysts supported on various metal oxides, *J. Catal.* 343 (2016) 178–184. <https://doi.org/10.1016/j.jcat.2016.07.018>.
- [45] Y. Zhan, Y. Wang, D. Gu, C. Chen, L. Jiang, K. Takehira, Ni/Al<sub>2</sub>O<sub>3</sub>-ZrO<sub>2</sub> catalyst for CO<sub>2</sub> methanation: The role of  $\gamma$ -(Al, Zr)<sub>2</sub>O<sub>3</sub> formation, *Appl. Surf. Sci.* 459 (2018) 74–79. <https://doi.org/10.1016/j.apsusc.2018.07.206>.
- [46] A. Quindimil, U. De-La-Torre, B. Pereda-Ayo, J.A. González-Marcos, J.R. González-Velasco, Ni catalysts with La as promoter supported over Y- and BETA- zeolites for CO<sub>2</sub> methanation, *Appl. Catal. B Environ.* 238 (2018) 393–403. <https://doi.org/10.1016/j.apcatb.2018.07.034>.
- [47] W.L. Vrijburg, E. Moiola, W. Chen, M. Zhang, B.J.P. Terlingen, B. Zijlstra, I.A.W. Filot, A. Züttel, E.A. Pidko, E.J.M. Hensen, Efficient Base-Metal NiMn/TiO<sub>2</sub> Catalyst for CO<sub>2</sub>

- Methanation, *ACS Catal.* 9 (2019) 7823–7839. <https://doi.org/10.1021/acscatal.9b01968>.
- [48] J. Li, Y. Zhou, X. Xiao, W. Wang, N. Wang, W. Qian, W. Chu, Regulation of Ni-CNT Interaction on Mn-Promoted Nickel Nanocatalysts Supported on Oxygenated CNTs for CO<sub>2</sub> Selective Hydrogenation, *ACS Appl. Mater. Interfaces.* 10 (2018) 41224–41236. <https://doi.org/10.1021/acscami.8b04220>.
- [49] W. Zhen, F. Gao, B. Tian, P. Ding, Y. Deng, Z. Li, H. Gao, G. Lu, Enhancing activity for carbon dioxide methanation by encapsulating (1 1 1) facet Ni particle in metal–organic frameworks at low temperature, *J. Catal.* 348 (2017) 200–211. <https://doi.org/10.1016/j.jcat.2017.02.031>.
- [50] C. Hu, J. Qu, Y. Xiao, S. Zhao, H. Chen, L. Dai, Carbon Nanomaterials for Energy and Biorelated Catalysis: Recent Advances and Looking Forward, *ACS Cent. Sci.* 5 (2019) 389–408. <https://doi.org/10.1021/acscentsci.8b00714>.
- [51] W. Wang, C. Duong-Viet, H. Ba, W. Baaziz, G. Tuci, S. Caporali, L. Nguyen-Dinh, O. Ersen, G. Giambastiani, C. Pham-Huu, Nickel Nanoparticles Decorated Nitrogen-Doped Carbon Nanotubes (Ni/N-CNT); A Robust Catalyst for the Efficient and Selective CO<sub>2</sub> Methanation, *ACS Appl. Energy Mater.* 2 (2019) 1111–1120. <https://doi.org/10.1021/acsaem.8b01681>.
- [52] A. Primo, J. He, B. Jurca, B. Cojocaru, C. Bucur, V.I. Parvulescu, H. Garcia, CO<sub>2</sub> methanation catalyzed by oriented MoS<sub>2</sub> nanoplatelets supported on few layers graphene, *Appl. Catal. B Environ.* 245 (2019) 351–359. <https://doi.org/10.1016/j.apcatb.2018.12.034>.
- [53] I. Janowska, M.S. Moldovan, O. Ersen, H. Bulou, K. Chizari, M.J. Ledoux, C. Pham-Huu, High temperature stability of platinum nanoparticles on few-layer graphene investigated by In Situ high resolution transmission electron microscopy, *Nano Res.* 4 (2011) 511–521. <https://doi.org/10.1007/s12274-011-0107-z>.
- [54] H. Vedala, D.C. Sorescu, G.P. Kotchey, A. Star, Chemical sensitivity of graphene edges decorated with metal nanoparticles, *Nano Lett.* 11 (2011) 2342–2347. <https://doi.org/10.1021/nl2006438>.
- [55] D. Mateo, J. Albero, H. García, Graphene supported NiO/Ni nanoparticles as efficient photocatalyst for gas phase CO<sub>2</sub> reduction with hydrogen, *Appl. Catal. B Environ.* 224 (2018) 563–571. <https://doi.org/10.1016/j.apcatb.2017.10.071>.
- [56] F. Hu, S. Tong, K. Lu, C.M. Chen, F.Y. Su, J. Zhou, Z.H. Lu, X. Wang, G. Feng, R. Zhang, Reduced graphene oxide supported Ni-Ce catalysts for CO<sub>2</sub> methanation: The support and ceria promotion effects, *J. CO<sub>2</sub> Util.* 34 (2019) 676–687. <https://doi.org/10.1016/j.jcou.2019.08.020>.
- [57] W. Wang, G. Tuci, C. Duong-Viet, Y. Liu, A. Rossin, L. Luconi, J.M. Nhut, L. Nguyen-Dinh, C. Pham-Huu, G. Giambastiani, Induction Heating: An Enabling Technology for the Heat Management in Catalytic Processes, *ACS Catal.* 9 (2019) 7921–7935. <https://doi.org/10.1021/acscatal.9b02471>.

- [58] S.R. Yassine, Z. Fatfat, G.H. Darwish, P. Karam, Localized catalysis driven by the induction heating of magnetic nanoparticles, *Catal. Sci. Technol.* 10 (2020) 3890–3896. <https://doi.org/10.1039/d0cy00439a>.
- [59] D. De Masi, J.M. Asensio, P. Fazzini, L. Lacroix, B. Chaudret, Engineering Iron–Nickel Nanoparticles for Magnetically Induced CO<sub>2</sub> Methanation in Continuous Flow, *Angew. Chemie Int. Ed.* 59 (2020) 6187–6191. <https://doi.org/10.1002/anie.201913865>.
- [60] W. Wang, C. Duong-Viet, Z. Xu, H. Ba, G. Tuci, G. Giambastiani, Y. Liu, T. Truong-Huu, J.M. Nhut, C. Pham-Huu, CO<sub>2</sub> methanation under dynamic operational mode using nickel nanoparticles decorated carbon felt (Ni/OCF) combined with inductive heating, *Catal. Today.* 357 (2020) 214–220. <https://doi.org/10.1016/j.cattod.2019.02.050>.
- [61] W. Wang, C. Duong-Viet, G. Tuci, Y. Liu, A. Rossin, L. Luconi, J. Nhut, L. Nguyen-Dinh, G. Giambastiani, C. Pham-Huu, Cover Feature: Highly Nickel-Loaded  $\gamma$ -Alumina Composites for a Radiofrequency-Heated, Low-Temperature CO<sub>2</sub> Methanation Scheme (*ChemSusChem* 20/2020), *ChemSusChem.* 13 (2020) 5341–5341. <https://doi.org/10.1002/cssc.202002150>.
- [62] A.A. Balandin, S. Ghosh, W. Bao, I. Calizo, D. Teweldebrhan, F. Miao, C.N. Lau, Superior Thermal Conductivity of Single-Layer Graphene, *Nano Lett.* 8 (2008) 902–907. <https://doi.org/10.1021/nl0731872>.
- [63] H. Ba, L. Truong-Phuoc, C. Pham-Huu, W. Luo, W. Baaziz, T. Romero, I. Janowska, Colloid Approach to the Sustainable Top-Down Synthesis of Layered Materials, *ACS Omega.* 2 (2017) 8610–8617. <https://doi.org/10.1021/acsomega.7b01311>.
- [64] W. Brockner, C. Ehrhardt, M. Gjika, Thermal decomposition of nickel nitrate hexahydrate, Ni(NO<sub>3</sub>)<sub>2</sub>·6H<sub>2</sub>O, in comparison to Co(NO<sub>3</sub>)<sub>2</sub>·6H<sub>2</sub>O and Ca(NO<sub>3</sub>)<sub>2</sub>·4H<sub>2</sub>O, *Thermochim. Acta.* 456 (2007) 64–68. <https://doi.org/https://doi.org/10.1016/j.tca.2007.01.031>.
- [65] B. Małeczka, A. Łącz, E. Drożdż, A. Małeczki, Thermal decomposition of d-metal nitrates supported on alumina, *J. Therm. Anal. Calorim.* 119 (2015) 1053–1061. <https://doi.org/10.1007/s10973-014-4262-9>.
- [66] E.A. Périgo, G. Hemery, O. Sandre, D. Ortega, E. Garaio, F. Plazaola, F.J. Teran, Fundamentals and advances in magnetic hyperthermia, *Appl. Phys. Rev.* 2 (2015) 41302. <https://doi.org/10.1063/1.4935688>.
- [67] F. Perton, M. Tasso, G.A. Muñoz Medina, M. Ménard, C. Blanco-Andujar, E. Portiansky, M.B.F. van Raap, D. Bégin, F. Meyer, S. Begin-Colin, D. Mertz, Fluorescent and magnetic stellate mesoporous silica for bimodal imaging and magnetic hyperthermia, *Appl. Mater. Today.* 16 (2019) 301–314. <https://doi.org/https://doi.org/10.1016/j.apmt.2019.06.006>.
- [68] A. Adam, K. Parkhomenko, P. Duenas-Ramirez, C. Nadal, G. Cotin, P.-E. Zorn, P. Choquet, S. Bégin-Colin, D. Mertz, Orienting the Pore Morphology of Core-Shell Magnetic Mesoporous Silica with the Sol-Gel Temperature. Influence on MRI and Magnetic

- Hyperthermia Properties, *Mol. .* 26 (2021). <https://doi.org/10.3390/molecules26040971>.
- [69] A. Mohanty, W. Baaziz, M. Lafjah, V. Da Costa, I. Janowska, Few layer graphene as a template for Fe-based 2D nanoparticles, *FlatChem.* 9 (2018) 15–20. <https://doi.org/10.1016/j.flatc.2018.04.002>.
- [70] X. Lin, S. Wang, W. Tu, Z. Hu, Z. Ding, Y. Hou, R. Xu, W. Dai, MOF-derived hierarchical hollow spheres composed of carbon-confined Ni nanoparticles for efficient CO<sub>2</sub> methanation, *Catal. Sci. Technol.* 9 (2019) 731–738. <https://doi.org/10.1039/c8cy02329h>.
- [71] Y. Zhang, Y. Shen, X. Xie, W. Du, L. Kang, Y. Wang, X. Sun, Z. Li, B. Wang, One-step synthesis of the reduced graphene oxide@NiO composites for supercapacitor electrodes by electrode-assisted plasma electrolysis, *Mater. Des.* 196 (2020) 109111. <https://doi.org/10.1016/j.matdes.2020.109111>.
- [72] I. Champon, A. Bengaouer, A. Chaise, S. Thomas, A.-C. Roger, Carbon dioxide methanation kinetic model on a commercial Ni/Al<sub>2</sub>O<sub>3</sub> catalyst, *J. CO<sub>2</sub> Util.* 34 (2019) 256–265. <https://doi.org/https://doi.org/10.1016/j.jcou.2019.05.030>.
- [73] X. Guo, A. Traitangwong, M. Hu, C. Zuo, V. Meeyoo, Z. Peng, C. Li, Carbon Dioxide Methanation over Nickel-Based Catalysts Supported on Various Mesoporous Material, *Energy and Fuels.* 32 (2018) 3681–3689. <https://doi.org/10.1021/acs.energyfuels.7b03826>.
- [74] K. Stangeland, D.Y. Kalai, H. Li, Z. Yu, Active and stable Ni based catalysts and processes for biogas upgrading: The effect of temperature and initial methane concentration on CO<sub>2</sub> methanation, *Appl. Energy.* 227 (2018) 206–212. <https://doi.org/10.1016/j.apenergy.2017.08.080>.
- [75] F. Koschany, D. Schlereth, O. Hinrichsen, On the kinetics of the methanation of carbon dioxide on coprecipitated NiAl(O)<sub>x</sub>, *Appl. Catal. B Environ.* 181 (2016) 504–516. <https://doi.org/10.1016/j.apcatb.2015.07.026>.
- [76] M. Frey, T. Romero, A.C. Roger, D. Edouard, Open cell foam catalysts for CO<sub>2</sub> methanation: Presentation of coating procedures and in situ exothermicity reaction study by infrared thermography, *Catal. Today.* 273 (2016) 83–90. <https://doi.org/10.1016/j.cattod.2016.03.016>.
- [77] A. Yamaguchi, E. Iglesia, Catalytic activation and reforming of methane on supported palladium clusters, *J. Catal.* 274 (2010) 52–63. <https://doi.org/10.1016/j.jcat.2010.06.001>.
- [78] K. Aasberg-Petersen, J.H. Bak Hansen, T.S. Christensen, I. Dybkjaer, P.S. Christensen, C. Stub Nielsen, S.E.L. Winter Madsen, J.R. Rostrup-Nielsen, Technologies for large-scale gas conversion, *Appl. Catal. A Gen.* 221 (2001) 379–387. [https://doi.org/10.1016/S0926-860X\(01\)00811-0](https://doi.org/10.1016/S0926-860X(01)00811-0).
- [79] S.E. Olesen, K.J. Andersson, C.D. Damsgaard, I. Chorkendorff, Deactivating Carbon Formation on a Ni/Al<sub>2</sub>O<sub>3</sub> Catalyst under Methanation Conditions, *J. Phys. Chem. C.* 121 (2017) 15556–15564. <https://doi.org/10.1021/acs.jpcc.7b03754>.
- [80] C. Mebrahtu, S. Abate, S. Perathoner, S. Chen, G. Centi, CO<sub>2</sub> methanation over Ni catalysts

based on ternary and quaternary mixed oxide: A comparison and analysis of the structure-activity relationships, *Catal. Today.* 304 (2018) 181–189. <https://doi.org/10.1016/j.cattod.2017.08.060>.

- [81] J. Gao, Y. Wang, Y. Ping, D. Hu, G. Xu, F. Gu, F. Su, A thermodynamic analysis of methanation reactions of carbon oxides for the production of synthetic natural gas, *RSC Adv.* 2 (2012) 2358–2368. <https://doi.org/10.1039/c2ra00632d>.
- [82] A.A. Balandin, Thermal properties of graphene and nanostructured carbon materials, *Nat. Mater.* 10 (2011) 569–581. <https://doi.org/10.1038/nmat3064>.
- [83] S. Ghosh, W. Bao, D.L. Nika, S. Subrina, E.P. Pokatilov, C.N. Lau, A.A. Balandin, Dimensional crossover of thermal transport in few-layer graphene, *Nat. Mater.* 9 (2010) 555–558. <https://doi.org/10.1038/nmat2753>.